

*Modeling the impacts of urbanization and open water surface on heavy convective rainfall: a case study over the emerging Xiong'an city, China*

Article

Accepted Version

Xing, Y., Ni, G., Yang, L., Yang, Y., Xing, P. and Sun, T.  
ORCID: <https://orcid.org/0000-0002-2486-6146> (2019)  
Modeling the impacts of urbanization and open water surface on heavy convective rainfall: a case study over the emerging Xiong'an city, China. *Journal of Geophysical Research: Atmospheres*, 124 (16). pp. 9078-9098. ISSN 2169-8996 doi: <https://doi.org/10.1029/2019JD030359> Available at <https://centaur.reading.ac.uk/85445/>

It is advisable to refer to the publisher's version if you intend to cite from the work. See [Guidance on citing](#).

To link to this article DOI: <http://dx.doi.org/10.1029/2019JD030359>

Publisher: American Geophysical Union

All outputs in CentAUR are protected by Intellectual Property Rights law, including copyright law. Copyright and IPR is retained by the creators or other copyright holders. Terms and conditions for use of this material are defined in the [End User Agreement](#).

[www.reading.ac.uk/centaur](http://www.reading.ac.uk/centaur)

**CentAUR**

Central Archive at the University of Reading

Reading's research outputs online

1           **Modeling the Impacts of Urbanization and Open Water Surface on Heavy**  
2           **Convective Rainfall: A Case Study over the Emerging Xiong'an City, China**

3           **Yue Xing<sup>1</sup>, Guangheng Ni<sup>1</sup>, Long Yang<sup>2,3\*</sup>, Yan Yang<sup>1</sup>, Pei Xing<sup>4</sup> and Ting Sun<sup>5</sup>**

4           <sup>1</sup>State Key Laboratory of Hydro-Science and Engineering, Department of Hydraulic  
5           Engineering, Tsinghua University, Beijing 100084, China

6           <sup>2</sup>School of Geography and Ocean Science, Nanjing University, Nanjing 210023, Jiangsu  
7           Province, China

8           <sup>3</sup>Department of Civil and Environmental Engineering, Princeton University, Princeton, NJ, USA

9           <sup>4</sup>Beijing Municipal Climate Center, Beijing 100089, China

10          <sup>5</sup>Department of Meteorology, University of Reading, Reading, RG6 6BB, UK

11          Corresponding author: Long Yang (yanglong86123@hotmail.com)

12          **Key Points:**

- 13           • Open water surface and urbanization show contrasting impact on heavy rainfall under  
14           strong large-scale forcing.
- 15           • Changes in rainfall accumulation highlight strong dependence of urban-induced rainfall  
16           anomalies on urbanization stages.
- 17           • Interactions between open water and urban surface contribute to downwind rainfall  
18           enhancement through intensified moist convection.
- 19

## 20 **Abstract**

21 In this study, we examine the impacts of urbanization and open water surface on heavy  
22 convective rainfall based on numerical modeling experiments using the Weather Research and  
23 Forecasting (WRF) model. We focus on a severe storm event over the emerging Xiong'an city in  
24 northern China. The storm event consists of two episodes, and features intense moisture transport  
25 and strong large-scale forcing. A set of WRF simulations were implemented to examine the  
26 sensitivity of spatiotemporal rainfall variability in and around the urban area to different land use  
27 scenarios. Modeling results highlight contrasting roles of open water and urban surface in  
28 dictating space-time organizations of convective rainfall under strong large-scale forcing.  
29 Dynamic perturbation to atmospheric forcing dominates the impacts of open water and urban  
30 surface on spatial rainfall distribution during the second storm episode, while urban surface  
31 promotes early initiation of convection during the first storm episode through enhanced buoyant  
32 energy. Open water surface contributes to convective inhibition through evaporative cooling but  
33 can enhance moist convection when the impact of urban surface is also considered. The  
34 synergistic effect of open water and urban surface leads to rainfall enhancement both over and in  
35 the downwind urban area. Changes in rainfall accumulation with different spatial extents of  
36 urban coverage highlight strong dependence of urban-induced rainfall anomalies on urbanization  
37 stages. Our results provide improved understandings on hydrometeorological impacts due to  
38 emerging cities in complex physiographic settings, and emphasize the importance of atmospheric  
39 forcing in urban rainfall modification studies.

## 40 **1 Introduction**

41 The impact of urbanization on rainfall has been extensively examined following the  
42 METROpolitan Meteorological Experiment (METROMEX, e.g., Changnon et al., 1971;  
43 Changnon et al., 1976) since the late 1970s. Modeling and observational studies show that  
44 urbanization has induced detectable rainfall anomalies both over and in the downwind urban  
45 areas (e.g., Ashley et al., 2012; Miao et al., 2009, 2011; Niyogi et al., 2011; Shepherd, 2005;  
46 Shepherd et al., 2002; Yang, et al., 2014a, 2014b; Yeung et al., 2015). There are three physical  
47 mechanisms associated with the phenomenon: (1) the “Urban Heat Island” effect increases  
48 surface temperature and promotes convection within the atmospheric boundary layer over urban  
49 areas (e.g., Bornstein & Lin, 2000; Collier, 2006; Dixon & Mote, 2003; Miao et al., 2009; Nie et  
50 al., 2017; Qiao et al., 2019; Souma et al., 2013); (2) increased surface roughness over urban  
51 canopy facilitates convergence (e.g., Loose & Bornstein, 1977; Shem & Shepherd, 2009); (3)  
52 urban aerosols influence rainfall microphysical processes through modifications on the physical  
53 and statistical properties of cloud condensation nuclei (e.g., Jin & Dickinson, 2010; Jin et al.,  
54 2005; Ntelekos et al., 2009).

55 Despite existing research results, our understanding of rainfall modification by urban  
56 environments is far from complete, especially for heavy convective rainfall under strong large-  
57 scale forcing (e.g., monsoon, extratropical system, tropical cyclone) (Paul et al., 2018; Reames &  
58 Stensrud, 2018; Singh et al., 2016; Zhang et al., 2018). For instance, Yang et al. (2014a)  
59 investigated the impact of urbanization on a severe thunderstorm under strong large-scale forcing  
60 over Milwaukee-Lake Michigan region. Their analyses show urbanization does not change cloud  
61 structure at regional scales but can modify space-time organizations of extreme rainfall around  
62 the city. Heavy convective rainfall under strong large-scale forcing is responsible for severe  
63 flooding over urban areas, which is a major concern in recent decades under the context of rapid

64 urbanization and booming urban population all over the world. McLeod et al. (2017) highlight  
65 the importance of considering flow regimes in urban rainfall modification studies based on  
66 climatological analyses of spatial-temporal rainfall patterns over Atlanta, Georgia. It is an  
67 important issue for storm cases with strong large-scale forcing since flow regimes determine key  
68 features of the pre-storm environment as well as advection of moisture that feeds the storm. In  
69 this study, we focus on heavy convective rainfall with contrasting flow regimes under strong  
70 large-scale forcing.

71 Urban impacts on rainfall for cities in complex physiographic settings (e.g., land-water  
72 boundaries, complex terrain) are still poorly understood due to the complexity of topography-  
73 related circulations and urban effects (e.g., Fernando, 2010; Freitag et al., 2018; Ganbat et al.,  
74 2015; Lin et al., 2011; Ryu et al., 2016; Shepherd et al., 2010). In this study, we focus on cities  
75 that are characterized by distinct land-water boundaries (i.e., lake). The impact of open water  
76 surface on rainfall and regional climate has been extensively examined in previous studies (e.g.,  
77 Anyah et al., 2006; Chuang & Sousounis, 2003; Laird et al., 2009; Long et al., 2007; Notaro et  
78 al., 2013; Sousounis & Mann, 2000; Stivari et al., 2003; Sun et al., 2015; Wilson, 1977). The  
79 evaporative cooling effect of open water surface leads to a stable atmospheric boundary layer  
80 that inhibits convection and rainfall (e.g., Changnon, 1984; Farley Nicholls & Toumi, 2014). Gu  
81 et al. (2016) found that the impact of lake on local summer precipitation is negative during the  
82 day, and is positive during the night. The presence of urban areas by lakeside can enhance  
83 thermodynamic contrast between land and water that generate complex interactions between the  
84 lake-land breeze and urban-induced circulation. The evolution speed and penetration depth of  
85 lake-land breeze front can be greatly enhanced due to the presence of cities (e.g., Carter et al.,  
86 2012; Lin et al., 2008; Lo et al., 2007; Ohashi & Kida, 2002). For instance, Yang et al. (2014a)  
87 found that thermodynamic perturbation induced by urban surface enhances the intrusion of lake  
88 breeze and promotes the formation of a convergence zone over the northern boundary of  
89 Milwaukee (by the side of Lake Michigan) (similarly see, e.g., Shepherd & Burian, 2003;  
90 Shepherd et al., 2010 for studies over Houston). Unlike previous studies that focus on cities in  
91 the vicinity of an open water surface with a large spatial extent (i.e., typically lakes or oceans),  
92 we consider cities with a water body of its spatial extent less than or comparable to the size of  
93 the city itself. Theeuwes et al. (2013) modeled the influence of open water surfaces on  
94 summertime temperature and thermal comfort within a city. Open water surface contributes to  
95 both evaporative cooling for convective inhibition and additional moisture sources for moist  
96 convection, which demonstrates sharp contrast to the urban impact on convective rainfall. In this  
97 study, we shed light on the interrelated roles of contrasting thermodynamic and dynamic  
98 properties between open water and urban surface in dictating spatial and temporal variability of  
99 heavy convective rainfall.

100 Our study region is the emerging Xiong'an New Area (XNA, Figure 1), a new national-  
101 level district initiated by the Chinese government in 2017 to form the Beijing-Tianjin-Hebei  
102 (BTH) economic triangle for coordinated regional development. The initial urban coverage for  
103 XNA is 100 km<sup>2</sup> with a projected extent of 200 km<sup>2</sup> for its mid-term development. In the long  
104 run, Xiong'an city will be developed into a metropolis of 2000 km<sup>2</sup> (a comparable spatial extent  
105 of Beijing). It is noted the Baiyang Lake, an open water surface of 360 km<sup>2</sup> in XNA, may have  
106 potential impact on regional hydrometeorological processes. Improved understandings on the  
107 impact are thus critical for better regional planning of the BTH economic triangle.

108 The main objective of this study is to examine the impacts of open water and  
109 urbanization on heavy convective rainfall under strong large-scale forcing. Extreme rainfall over  
110 the study region is frequently associated with interactions of mid-latitude weather systems and  
111 moisture transport during the East Asian Summer Monsoon period. We focus on a severe storm  
112 event on 20 July 2016 over northern China. Our analyses are principally motivated by the  
113 following hypotheses: (1) contrasting impacts of open water and urban surface on spatiotemporal  
114 rainfall variability originate from thermodynamic and dynamic contrasts of surface properties as  
115 well as synoptic flow regimes; (2) cumulative rainfall over XNA and in the downwind region  
116 increases with the expanding spatial extent of urban coverage; (3) open water surface  
117 synergistically enhances moist convection with urban surface when the spatial extent of two  
118 surfaces are comparable. We examine these hypotheses based on high-resolution numerical  
119 simulations using a non-hydrostatic, fully comprehensible, mesoscale meteorological model,  
120 Weather Research and Forecasting (WRF) (Skamarock et al., 2008), with contrasting land  
121 use/land cover configurations.

122 The rest of the paper is organized as follows. In section 2, we describe observations,  
123 model configurations as well as details of the experiment setup. Results and discussions are  
124 provided in section 3, followed by section 4 for summary and conclusions.

## 125 **2 Data and Methodology**

### 126 2.1 Observations

127 We use three types of observations to evaluate the model performance:

128 a) Hourly observations of 2-m air temperature, 2-m relative humidity, 10-m wind speed,  
129 rain rate collected at 30 national weather stations (see Figure 1 for site locations) quality-  
130 controlled by CMA (Chinese Meteorological Administration) to examine the near-surface  
131 meteorology.

132 b) Hourly fusion precipitation product of automatic station and CMORPH (CPC  
133 MORPHing technique) at a spatial resolution of 0.1 degree to characterize the spatiotemporal  
134 rainfall variability (e.g., Chun-Hua et al., 2014).

135 c) Radiosonde observations of temperature, mixing ratio and wind speed (see Figure 1 for  
136 site location) to investigate the vertical profiles of synoptic conditions before and during the  
137 storm event.

### 138 2.2 Model configuration

139 The Advanced Research version WRF (ARW) version 3.7 is used in this study. The study  
140 area XNA is represented in three two-way nested domains (spatial extents of 200×200, 220×220  
141 and 187×211 horizontal grids, with the corresponding resolution of 9 km, 3 km, and 1 km,  
142 respectively; Figure 1a). The outermost domain covers most of the central and northeastern  
143 China, while the innermost domain covers XNA and its surrounding region, including the  
144 southern part of Beijing and the western part of Tianjin (Figure 1b). The grids contain 54 sigma  
145 levels, with the upper boundary set at 50 hPa. The integral time step for the outer domain is 15 s.  
146 The initial and boundary conditions are provided by the National Center for Environmental  
147 Prediction (NCEP) Global Final Analysis (FNL) at a spatial and temporal resolution of 1 degree

148 and 6 hours, respectively. The 21-category MODIS dataset is used to represent land use and land  
149 cover in the study region.

150 Previous studies show that rainfall simulations are very sensitive to microphysics  
151 schemes adopted in atmospheric models, with planetary boundary layer scheme, radiation  
152 scheme, and other parameterizations playing a relatively smaller role (e.g., Efstathiou et al.,  
153 2013; Liu et al., 2011; Singh et al., 2018). We carried out sensitivity experiments over the study  
154 region for the 20 July 2016 storm (see section 3.1 for detailed descriptions of the case) with  
155 WRF simulations using different microphysics schemes, including WSM3, WSM5, and WSM6.  
156 The WRF simulation with WSM5 (Hong et al., 2004) shows the best performance against  
157 observations (not shown): we thus choose WSM5 as the microphysical parametrization in our  
158 following experiments. The other physics options configured in the model include: the MYJ  
159 planetary boundary layer (PBL) scheme (Janjić, 1994), the Dudhia shortwave radiation scheme  
160 (Dudhia, 1989), the Rapid Radiative Transfer Model (RRTM) longwave radiation scheme  
161 (Mlawer et al., 1997), Noah land surface model (Chen & Dudhia, 2001) and Monin-Obukhov  
162 Surface Layer scheme (Monin & Obukhov, 1954). Cumulus scheme is turned off for all domains  
163 due to the fine spatial resolution of horizontal grids (less than 10 km, e.g., Stensrud, 2009). In  
164 this study, we incorporate the multi-layer lake scheme by Subin et al. (2012) in WRF (Gu et al.,  
165 2015) to accurately depict the variations of heat, moisture, and momentum over the Baiyang  
166 Lake. In addition, the single-layer Urban Canopy Model (UCM) in WRF (see Chen et al., 2011  
167 for details) is also used to accurately represent the thermal and dynamic properties of urban land  
168 surfaces with the default UCM parameters. Table 1 provides a summary of all key physics  
169 schemes used in WRF simulations of this study.

### 170 2.3 Experimental setup

171 To assess the urban-lake effects six WRF scenarios are set up (Table 2):

172 a) *control* scenario (CTRL, Figure 2a): Only the Baiyang Lake is considered with a small  
173 portion of urban coverage distributed to the southeast of the Lake, representing the present land  
174 use conditions over this region. This scenario is compared against in-situ observations to  
175 evaluate model performance (see section 3.2).

176 b) *urban* scenario (URB, Figure 2b): Baiyang Lake is set as in CTRL with its surrounding  
177 rural area replaced by urban surfaces, representing the maximum urbanization extent over XNA.

178 c) *baseline* scenario (BASE, Figure 2c): Baiyang Lake is removed from the CTRL  
179 scenario by replacing the water surface with cropland (i.e., the dominant land use type  
180 surrounding the city). Comparisons between CTRL/URB and BASE scenarios will be used to  
181 examine the impacts of open water and urban surface on rainfall.

182 d) Three other development scenarios of XNA (ULS, ULM, and ULL, Figure 2d, 2e and  
183 2f, respectively): these additional urbanization scenarios (ULS, ULM, and ULL, with 120, 410,  
184 and 1417 urban grids, respectively; the total sizes are summarized in Table 2), are set up by  
185 replacing the outskirts of Baiyang Lake with cropland to mimic projected developments of XNA.

186 All the numerical experiments adopt the same model configurations as depicted in section  
187 2.2 and summarized in Table 1, with land use/land cover being the only model difference. All the  
188 simulations are initiated at 00 UTC 17 July 2016 and run till 00 UTC 22 July 2016. The first 40  
189 hours are regarded as model spin-up and are not included in the following analyses.

### 190 3 Results and Discussion

#### 191 3.1 Synoptic background of 20 July 2016 storm

192 The 20 July 2016 storm persisted for more than 40 hours and produced widespread  
193 extreme rainfall over Beijing, Tianjin, and Hebei province. Nine state-level weather stations in  
194 Beijing recorded history-breaking rain rates (Gan et al., 2017). The maximum hourly rain rate is  
195  $56.8 \text{ mm h}^{-1}$ . Maximum rainfall accumulation is 454 mm. The 20 July 2016 storm is associated  
196 with the evolution of a cold vortex and its interactions with the East Asian Summer Monsoon  
197 system. The pre-storm environment is characterized by strong moisture transport driven by the  
198 West Pacific Subtropical High that brings abundant warm and moist air plume to northern China.  
199 Meanwhile, the cold vortex gradually evolves from northwest to northern China, with cold air  
200 running down from the north (Figure 3). The low-pressure system promotes mesocyclogenesis  
201 and convection that leads to development of several mesoscale convective systems in northern  
202 China. Convective available potential energy (CAPE) is  $872 \text{ J kg}^{-1}$  at 00 UTC 19 July based on  
203 the radiosonde observation. Surface mixing ratio is around  $18 \text{ g kg}^{-1}$  at 12 UTC 19 UTC. The  
204 cold-air intrusion increases the baroclinicity of the atmosphere and serves as a strong catalyst for  
205 strong convection over the study region. The strengthening subtropical high and its extension to  
206 inland China “block” the track of the cold vortex, and ultimately provide a favorable  
207 environment for long-lasting convective outbreaks and extreme rainfall over northern China.  
208 Mesoscale topography (i.e., the Taihang Mountains to the northwest of domain 3) also plays a  
209 role in maintaining and enhancing convective intensity. There is a local maximum of wind speed  
210 over  $20 \text{ m s}^{-1}$  around the altitude of 1 km around 00 UTC 20 July (before the peak rain rates) ,  
211 indicating that low-level jet as an additional ingredient for the 20 July 2016 storm.

212 The storm event consists of two storm episodes with changing synoptic flow regimes.  
213 The first storm episode (from 20 UTC 18 July to 14 UTC 19 July) is characterized with steering  
214 level wind blowing from the southwest. There is only moderate rainfall over XNA during the  
215 first storm episode. The second storm episode (from 15 UTC 19 July to 13 UTC 20 July) is  
216 dominated by southerly/southeasterly flow with relatively larger wind speeds (i.e., strong  
217 forcing), and produces intense rainfall over XNA. Contrasting synoptic flows determine the way  
218 how interactions of synoptic forcing and topography (i.e., the orientation is southwest towards  
219 northeast, see Figure 1b) influence spatiotemporal rainfall variability in the study region for the  
220 20 July 2016 storm.

#### 221 3.2 Model evaluation

222 The CTRL simulation captures variations of thermodynamic variables and wind fields  
223 during the entire period of the 20 July 2016 storm (Figure 4). The simulated 2-m temperature is  
224 in good agreement with observations before the rain starts, while it is underestimated after the  
225 rainfall peak with bias within a reasonable range (Figure 4a). The model generally captures the  
226 variation of relative humidity quite well, with slight underestimation (in terms of the median  
227 values) before and after rainfall (Figure 4b). The model reproduces key evolution features of  
228 surface wind fields during the entire simulation period, with slight overestimation after the  
229 peaking of rainfall (Figure 4c). Statistics, including Mean Bias, Root Mean Square Error  
230 (RMSE), correlation coefficient, and hit rate (HR) are calculated to quantitatively assess the  
231 model performance (Table 3): the hit rate for both 2-m temperature and rain rate exceeds 0.9;  
232 while correlation coefficient for 10-m wind speed is 0.78, indicating consistency between the

233 model simulation and in-situ observations. These statistics are comparable to previous studies  
234 (e.g., Zhang et al., 2017). Hourly rain rate peaks at around 22 UTC 19 July with a range from 10  
235  $\text{mm h}^{-1}$  to  $30 \text{ mm h}^{-1}$  (Figure 4d). The Mean Bias, RMSE and correlation between rain rate  
236 observation and simulation are 0.06, 4.67, and 0.58, respectively. Both the simulated peak timing  
237 and intensity of rainfall range agree well with the in-situ observations (Figure 4d). There is a  
238 strong rainband across Hebei province and extends to Tianjin at 22 UTC 19 July. The maximum  
239 hourly rain rate is approximately  $40 \text{ mm h}^{-1}$ . The rainband slowly propagates towards north and  
240 maintains peak rain rates till 02 UTC 20 July (Figure 5). The CTRL simulation captures the  
241 space-time organization of the rain band and evolution feature of slow propagation reasonably  
242 well, which are the key elements of extreme rainfall for the 20 July 2016 storm over the study  
243 region. The CTRL simulation captures the vertical profile of dynamic and thermodynamic  
244 variables before and during the storm (Figure 6). Even though there is a slight underestimation in  
245 terms of vertical wind profiles, both model and radiosonde observations show a “wind nose”  
246 around 1 km above the ground during the peak rainfall hour (00 UTC 20 July), with the wind  
247 speed exceeding  $20 \text{ m s}^{-1}$ .

248 In general, the CTRL simulation captures the spatiotemporal rainfall variability, key  
249 features of thermodynamic variables and wind fields for the 20 July 2016 storm reasonably well.  
250 Critical elements for extreme rainfall are also well represented in the simulation (e.g., low-level  
251 jet).

### 252 3.3 Impact on rainfall: open water versus urban surface

253 Different temporal evolutions of rain rate averaged over the entire XNA (see the black  
254 dashed box in Figure 1) are produced by the CTRL, BASE and URB simulations (Figure 7a).  
255 Compared to the CTRL simulation, the BASE simulation shows an earlier initiation of the  
256 second storm episode and produces less total rainfall over XNA region by 4 mm and 2 mm for  
257 the first and second storm episodes, respectively, indicating a positive influence of the open  
258 water surface on rainfall. The urban impact on rainfall is different from that of the lake. We  
259 notice an enhanced rainfall peak during the first storm episode in the URB simulation which  
260 contributes to increased total rainfall ( $\sim 32 \text{ mm}$ ), compared to the BASE simulation (Figure 7c).  
261 Three distinct “spikes” of hourly rain rates are noted during the second storm episode in the URB  
262 simulation, as opposed to the single dominant rainfall peak in either BASE or CTRL simulation  
263 (Figure 7a). However, the total rainfall over XNA is decreased by 12 mm in the URB simulation  
264 during the second storm episode compared to the BASE simulation (Figure 7c).

265 The spatial distribution of rainfall differences between CTRL, URB and BASE  
266 simulations is remarkable for the two storm episodes (Figure 8). Consistent with temporal  
267 evolution difference (cf. Figure 7a), the presence of the city increases rainfall over XNA during  
268 the first storm episode (Figure 8b). In addition to rainfall differences over XNA, strong rainfall  
269 enhancement is also observed over the upwind region for both the CTRL and URB simulation  
270 during the second storm episode, while only weak rainfall anomalies are scattered in either the  
271 upwind or downwind region for the first storm episode (Figure 8). Rainfall contrasts between the  
272 first and second storm episode highlight the importance of flow regimes in dictating  
273 hydrometeorological impacts due to land use/land cover changes. The opposite sign of rainfall  
274 changes during the second storm episode between CTRL and URB (Figure 7c) is associated with  
275 the thermodynamic contrasts of open water and urban surfaces, as will be further elaborated  
276 below.

277 Open water surface contributes to the increase in near-surface specific humidity ( $\sim 1 \text{ g kg}^{-1}$ ) and decrease in air temperature ( $\sim 0.5 \text{ K}$ ) through enhanced evaporation during the first storm  
278 episode (Figure 9a). As contrary in the URB simulation, we see a pronounced increase of near-  
279 surface temperature ( $\sim 1.5 \text{ K}$ ) over the entire urban coverage but mixed changes (i.e., both  
280 increase and decrease) in 2-m specific humidity (Figure 9b). Strong surface warming provides  
281 additional buoyant energy for convection over XNA that leads to earlier initiation of rainfall in  
282 the URB simulation (Figure 7a). Slight rainfall increase in the CTRL simulation is tied to  
283 elevated near-surface moisture over the lake, with the timing of rainfall kept the same as the  
284 BASE simulation (Figure 7a). Due to the large heat capacity of the water body, there is a slight  
285 increase in surface temperature ( $\sim 0.8 \text{ K}$ ) and specific humidity ( $\sim 0.5 \text{ g kg}^{-1}$ ) in the CTRL  
286 simulation compared to the BASE simulation after the first storm episode (Figure 9c). However,  
287 the city-induced surface warming effect is alleviated after the first storm episode in the URB  
288 simulation, with negligible temperature differences observed over XNA (Figure 9d).

290 In addition to the thermodynamic perturbations induced by open water and urban surface,  
291 noticeable perturbations exist in the near-surface wind fields due to increased (decreased) surface  
292 roughness in the URB (CTRL) simulation (Figure 9e-9h). Changes in the 10-m wind fields are  
293 consistent for both storm episodes with more significant changes for the second one. Increased  
294 surface roughness in the URB simulation reduces surface wind speed during the second storm  
295 episode, and creates an upwind convergence zone of XNA for increased rainfall (Figure 8d).  
296 Decreased rainfall over XNA during the second storm episode in the URB simulation is  
297 contributed by the depletion of atmospheric moisture content during the first storm episode and  
298 reduced moisture advection during the second storm episode.

299 We further examine the vertical wind profiles along the dominant wind vectors (Line AB  
300 and Line CD in Figure 8) for the two storm episodes (Figure 10), providing direct evidence that  
301 is responsible for the rainfall anomalies. For the first storm episode, the entire atmospheric  
302 column is characterized with a strong updraft over the urban area in the URB simulation, while  
303 for the CTRL simulation, updraft only exists in the lower atmosphere (below 1 km) underneath  
304 the downdraft over the lake. Without the lake or urban area (i.e., BASE simulation), there are  
305 stable horizontal wind vectors in the lower atmosphere with only a small updraft intensity before  
306 the rain. For the second storm episode, both the CTRL and URB simulations show enhanced  
307 updraft in the upwind boundary of the lake and urban area.

308 We provide moisture budget analysis for the storm event of all three simulations, i.e.,  
309 CTRL, URB, and BASE, in Figure 11a, 11b, and 11c. The overall contribution of evaporation is  
310 relatively small to total rainfall. In addition, evaporation is much smaller in the URB simulation  
311 than the other two simulations. Rainfall rates are consistently changed with convergence,  
312 indicating the role of moisture transport in determining rainfall intensity over XNA. Rainfall  
313 anomalies for the first storm episode are mainly due to thermodynamic perturbations induced by  
314 the presence of open water and urban surface. The thermodynamic contrast fades out after the  
315 first storm episode, and thus contributes marginally to rainfall changes over XNA region during  
316 the second storm episode. It is the strong atmospheric forcing with advection of unstable air  
317 plume that dominates the heavy rainfall process during the second storm episode. The increased  
318 (decreased) rainfall over the upwind (downwind) of XNA is mainly due to dynamic  
319 perturbations on atmospheric forcing that leads to bifurcation upwind of XNA. Rainfall  
320 anomalies (especially over XNA) induced by urban surface and the lake highlights contrasting  
321 roles of urban and water surface in modulating extreme rainfall events. We further investigate

322 the impacts of different spatial extents of urban coverages on spatiotemporal rainfall variability  
323 for the 20 July 2016 storm, with the influence of open water surface included.

### 324 3.4 Impact of urbanization on rainfall

325 Compared to the CTRL simulation, three urbanization simulations (i.e., ULS, ULM, and  
326 ULL) initiate earlier rainfall during the first storm episode (Figure 7b). Rainfall accumulation for  
327 both the first and second storm episode increases with the spatial extent of urban coverage over  
328 XNA, highlighting the strong dependence of urban-induced rainfall anomalies on urbanization  
329 stages (similarly see Miao et al., 2011). Comparisons between the three urbanization simulations  
330 and the CTRL simulation highlight the role of the open water surface in producing rainfall  
331 anomalies over XNA region associated with the expanding urban coverages. For instance,  
332 rainfall accumulation for the second storm episode in the ULL simulation (representing a full  
333 urbanization stage) is larger than the CTRL simulation by 10 mm. Given the role of urban  
334 surface in decreasing rainfall over XNA shown in the URB simulation (without the lake), we  
335 highlight that the presence of Baiyang lake increases rainfall over XNA through synergistic  
336 effects between open water and urban surface (Figure 7c).

337 We further show spatial distribution of rainfall differences for the two storm episodes  
338 between the three urbanization simulations and the CTRL simulation in Figure 12. In addition to  
339 rainfall changes over XNA, we find consistent rainfall increases in the downwind of XNA for  
340 both storm episodes. A monotonic rainfall enhancement is observed with urban coverage across  
341 the three urbanization simulations (Figure 12). The maximum rainfall increase appears ~100 km  
342 (~80 km) downwind of XNA for the first (second) storm episode; whereas such downwind  
343 rainfall enhancement is observed in neither CTRL nor URB (cf. Figure 8). Similar to the URB  
344 simulation, we see bifurcated low-level wind fields in the upwind of XNA, which contributes to  
345 decreased rainfall accumulation during the second storm episode for the ULS and ULM  
346 simulations. However, there is increased rainfall accumulation for the second storm episode in  
347 the ULL simulation compared to either CTRL or BASE (Figure 7c). We further show rainfall  
348 difference between the ULL and URB simulations in Figure 12. The only difference between the  
349 ULL and URB simulation is that the “lake-shaped” urban land surface in the URB simulation is  
350 replaced by open water surface (Figure 2 and Table 2). We find similar features of downwind  
351 rainfall enhancement, with relatively larger rainfall difference for both storm episodes in ULL  
352 than URB (Figure 12d and 12h), indicating the positive role of synergistic effects between open  
353 water and urban surface in determining rainfall anomalies over both XNA and its downwind  
354 region. A possible explanation is that the surface warming effect contributed by the urban  
355 surface facilitates moist convection together with the additional moisture availability contributed  
356 by open water surface (as elaborated in Section 3.3). The moist, unstable air plume advects  
357 downwind XNA region and leads to increased convective activity. Increased moisture advection  
358 is further confirmed in the moisture budget analysis: the peak convergence is  $36.8 \text{ mm h}^{-1}$  for  
359 ULL, while it is  $22.8 \text{ mm h}^{-1}$  and  $24.5 \text{ mm h}^{-1}$  for URB and CTRL, respectively (Figure 11d-f).

360 Figure 13 shows the differences in the spatial distribution of the thermodynamic and  
361 dynamic variables between the three urbanization simulations and the CTRL simulations.  
362 Expanding urban coverages contribute to increase near-surface air temperature over and  
363 surrounding the urban area: the average 2-m air temperature over urban areas is increased by 0.8  
364 K, 1.6 K, and 2 K in ULS, ULM and ULL, respectively. The temperature anomalies can extend  
365 up to 1.5 km above the ground in the three urbanization simulations (figures not shown),

366 indicating the urbanization-induced warming potential on the lower atmosphere. Changes in 2-m  
367 specific humidity vary with the expanding urban coverages. For instance, the ULM simulation  
368 presents the maximum increase in 2-m specific humidity by up to  $1.6 \text{ g kg}^{-1}$  over XNA, while  
369 only slight differences are produced by ULS and ULL (Figure 13a-13c). Changes of near-surface  
370 specific humidity are tied to moisture variations in the lower atmosphere. Like the URB  
371 simulation, we observe consistent decreases in 10-m wind speed with expanding urban coverages  
372 in the three urbanization simulations (Figure 13g-i).

373 Differences in thermodynamic and dynamic variables can lead to contrasting potentials  
374 for convection as indicated by Lifted index (LI, Figure 14). LI is the temperature difference  
375 between the environmental temperature at 500 hPa and the temperature of an air parcel lifted  
376 adiabatically from the surface to 500 hPa. LI is negative throughout the rainfall process,  
377 indicating that the atmosphere is unstable. Before the start of the first storm episode, LI is less  
378 than -5, indicating that the atmosphere is very unstable. LI can reach -7 to -8 near the city,  
379 indicating the impact of urban surface in promoting convection. The instability of the atmosphere  
380 is relatively weak in the scenario without city (Figure 14a and 14c) or with a smaller urban  
381 coverage (Figure 14d). After the first storm episode, the atmospheric instability is reduced (with  
382 LI around -3). The instability is comparatively higher for the scenarios with presence of urban or  
383 lake than the BASE simulation (Figure 14g, 14h, and 14j-14l).

384 We further characterize the pre-storm environment of both the first and second storm  
385 episode based on convective available potential energy and convective inhibition (CIN). Cross  
386 sections of CAPE along line AB (Figure 15) show increased values over the urban area. The  
387 region with CAPE exceeding  $900 \text{ J kg}^{-1}$  is confined within the lake zone, while it extends to  
388 downwind of XNA region for the three urbanization simulations. The CIN is decreased by  $10 \text{ J}$   
389  $\text{kg}^{-1}$  over the urban area. In addition, the positive CAPE penetrates to 4 km above the ground  
390 over urban areas for ULM and ULL, while for both CTRL and ULS, the atmospheric boundary  
391 layer is capped by an inversion layer at  $\sim 2 \text{ km}$  above the ground. Large CAPE indicates strong  
392 vertical velocities for convection, as can be seen from the vertical profiles of vertical velocity  
393 (Figure 16). Both ULM and ULL simulations show strong updraft over XNA, while for the ULL  
394 simulation, the updraft extends downwind of XNA. We can also see that strong convection  
395 enhances atmospheric moisture content (Figure 16, contour) in ULM and ULL. At the beginning  
396 of the second storm episode, CAPE in the ULS, ULM and ULL simulation is  $\sim 100 \text{ J kg}^{-1}$  larger  
397 than that in CTRL (Figure 15). Unlike the vertical wind profiles during the first storm episode,  
398 locations of updraft vary along the cross section during the second storm episode, even though  
399 we observe slightly larger vertical velocities in ULM and ULL (Figure 16f and 16h). Consistent  
400 updrafts are observed at 180 km along the cross section across the three urbanization and CTRL  
401 simulations, which are probably due to the forced lifting of regional topography to the northwest  
402 of XNA region (i.e., Taihang Mountains). Interactions between synoptic forcing and topography  
403 play an important role in rainfall enhancement over the downwind of XNA. The synoptic flow  
404 (southwesterly) aligns with the topography that minimizes its impact on rainfall anomalies  
405 during the first storm episode. Our results show rainfall anomalies induced by expanding urban  
406 coverages over XNA can extend to regional scales, and warrants particular attention for  
407 metropolis (e.g., Beijing) downwind from XNA.

## 408 **4 Summary and Conclusions**

409 In this study, we examined the 20 July 2016 storm that produced widespread flooding  
410 and extreme rainfall over northern China. Sensitivity simulations based on the WRF model  
411 (coupled with a lake Model and a single-layer urban canopy model) with contrasting land-use  
412 scenarios were implemented to investigate the impacts of open water surface (i.e., lake) and  
413 urbanization on spatiotemporal rainfall variability over the emerging Xiong'an (XNA) city in  
414 northern China. The main findings are summarized below.

415 (1) The 20 July 2016 storm is mainly attributed to interactions of a slowly-evolving cold  
416 vortex and moisture transport during the East Asian Summer Monsoon period. The storm event  
417 consists of two storm episodes with contrasting flow regimes, and is characterized with strong  
418 large-scale forcing (e.g., baroclinicity, LLJ). The CTRL simulation captures key elements of the  
419 20 July 2016 storm, including temporal variations of dynamic and thermodynamic fields during  
420 the entire storm period. The simulated spatiotemporal rainfall variability agrees well with  
421 CMORPH rainfall product and gauge observations.

422 (2) Model sensitivity experiments with different land surface configurations highlight  
423 contrasting roles of open water and urban surface in determining spatial and temporal  
424 organization of extreme rainfall. Urban surface provides additional buoyant energy that allows  
425 convection to occur earlier in the URB simulation than the CTRL simulation (with only the  
426 presence of the lake) during the first storm episode, while the open water surface contributes  
427 atmospheric moisture availability and increased rainfall over XNA. Dynamic perturbation (i.e.,  
428 changes in surface roughness) to atmospheric forcing dominates rainfall anomalies during the  
429 second storm episode for both URB and CTRL simulations. Rainfall contrasts between the two  
430 storm episodes highlight the importance of flow-regime analyses in understanding  
431 hydrometeorological impact due to land use/land cover changes.

432 (3) Changes in rainfall accumulation over XNA under different urbanization scenarios  
433 highlight strong dependence of urban-induced rainfall anomalies on the spatial extent of urban  
434 surfaces. The observed rainfall enhancement in the downwind of XNA for both storm episodes  
435 indicates that impacts of urbanization on rainfall are not confined within the proximity of urban  
436 areas, but can be transferred to regional scales.

437 (4) Comparisons between the URB (with the presence of only urban land surface) and  
438 ULL (with the presence of both urban and lake) simulations highlight the synergistic impacts of  
439 open water and urban surface on spatial rainfall distribution. The synergistic impact can be  
440 identified when the spatial extents of water surface and urban surface are comparable. The  
441 enhanced moist, unstable air plume contributed by evaporation from the open water and urban  
442 surface can be advected downwind of XNA region, and leads to intensified convection and  
443 rainfall.

444 Our modeling results highlight interrelated roles of contrasting land surface properties in  
445 dictating spatial and temporal variability of extreme rainfall, and contribute to improved  
446 understandings on hydrometeorological processes over complex physiographic settings. The  
447 emerging XNA in northern China is the showcase of dramatic anthropogenic modification on  
448 land use/land cover and provides opportunities to investigate its consequences on regional  
449 climate and extreme weather events associated with those changes. Numerical model  
450 experiments provide useful tools to look into the physical processes and guide city designs and  
451 regional planning. One limitation to appreciate is that a single storm event is analyzed in the

452 present study, and thus warrants caution of any generalization from the results. Future studies  
453 should include analyses of additional storm events with diverse synoptic conditions.

#### 454 **Acknowledgments**

455 YX, GN, and YY acknowledge the support from National Natural Science Foundation of China  
456 (51679119) and The National Key Research and Development Program of China  
457 (2018YFA0606002). TS acknowledges the support from NERC Independent Research  
458 Fellowship (NE/P018637/1). The WRF simulations were implemented on Tianhe-2 National  
459 Supercomputer Center in Guangzhou, China. Surface observational dataset is accessible from  
460 <http://www.urbanhydromet.org/en/>. The radiosonde observation is maintained by the University  
461 of Wyoming (<http://weather.uwyo.edu/upperair/sounding.html>). Precipitation fusion product of  
462 automatic station and CMORPH can be obtained from National Meteorological Information  
463 Center (<http://data.cma.cn/en>).

#### 464 **References**

- 465 Anyah, R. O., Semazzi, F. H., & Xie, L. (2006). Simulated physical mechanisms associated with  
466 climate variability over Lake Victoria basin in East Africa. *Monthly Weather Review*,  
467 134(12), 3588-3609. <https://doi.org/10.1175/MWR3266.1>
- 468 Ashley, W. S., Bentley, M. L., & Stallins, J. A. (2012). Urban-induced thunderstorm  
469 modification in the Southeast United States. *Climatic Change*, 113(2), 481-498.  
470 <https://doi.org/10.1007/s10584-011-0324-1>
- 471 Bornstein, R., & Lin, Q. (2000). Urban heat islands and summertime convective thunderstorms  
472 in Atlanta: Three case studies. *Atmospheric Environment*, 34(3), 507-516.  
473 [https://doi.org/10.1016/S1352-2310\(99\)00374-X](https://doi.org/10.1016/S1352-2310(99)00374-X)
- 474 Carter, M., Shepherd, J. M., Burian, S., & Jeyachandran, I. (2012). Integration of lidar data into a  
475 coupled mesoscale–land surface model: a theoretical assessment of sensitivity of urban–  
476 coastal mesoscale circulations to urban canopy parameters. *Journal of Atmospheric and  
477 Oceanic Technology*, 29(3), 328-346. <https://doi.org/10.1175/2011JTECHA1524.1>
- 478 Changnon Jr, S. A. (1984). Urban and lake effects on summer rainfall in the Chicago area.  
479 *Physical Geography*, 5(1), 1-23. <https://doi.org/10.1080/02723646.1984.10642240>
- 480 Changnon Jr, S. A., Huff, F. A., & Semonin, R. G. (1971). METROMEX: an investigation of  
481 inadvertent weather modification. *Bulletin of the American Meteorological Society*,  
482 52(10), 958-968. [https://doi.org/10.1175/1520-0477\(1971\)052<0958:MAIOIW>2.0.CO;2](https://doi.org/10.1175/1520-0477(1971)052<0958:MAIOIW>2.0.CO;2)
- 483 Changnon Jr, S. A., Semonin, R. G., & Huff, F. (1976). A hypothesis for urban rainfall  
484 anomalies. *Journal of Applied Meteorology*, 15(6), 544-560.  
485 [https://doi.org/10.1175/1520-0450\(1976\)015<0544:AHFURA>2.0.CO;2](https://doi.org/10.1175/1520-0450(1976)015<0544:AHFURA>2.0.CO;2)
- 486 Chen, F., & Dudhia, J. (2001). Coupling an advanced land surface–hydrology model with the  
487 Penn State–NCAR MM5 modeling system. Part I: Model implementation and sensitivity.  
488 *Monthly Weather Review*, 129(4), 569-585. [https://doi.org/10.1175/1520-0493\(2001\)129<0569:CAALSH>2.0.CO;2](https://doi.org/10.1175/1520-0493(2001)129<0569:CAALSH>2.0.CO;2)
- 490 Chen, F., Kusaka, H., Bornstein, R., Ching, J., Grimmond, C., Grossman-Clarke, S., et al.  
491 (2011). The integrated WRF/urban modelling system: development, evaluation, and

- 492 applications to urban environmental problems. *International Journal of Climatology*,  
493 31(2), 273-288. <https://doi.org/10.1002/joc.2158>
- 494 Chuang, H.-Y., & Sousounis, P. J. (2003). The impact of the prevailing synoptic situation on the  
495 lake-aggregate effect. *Monthly Weather Review*, 131(5), 990-1010.  
496 [https://doi.org/10.1175/1520-0493\(2003\)131<0990:TIOFPS>2.0.CO;2](https://doi.org/10.1175/1520-0493(2003)131<0990:TIOFPS>2.0.CO;2)
- 497 Chun-Hua, S., Dong, G., Hui, L., Bin, Z., & Ren-Qiang, L. (2014). Stratosphere-troposphere  
498 Exchange corresponding to a deep convection in the warm sector and abnormal  
499 subtropical front induced by a cutoff low over East Asia. *Chinese Journal of Geophysics*,  
500 57(1), 1-10. <https://doi.org/10.1002/cjg2.20079>
- 501 Collier, C. G. (2006). The impact of urban areas on weather. *Quarterly Journal of the Royal  
502 Meteorological Society*, 132(614), 1-25. <https://doi.org/10.1256/qj.05.199>
- 503 Dixon, P. G., & Mote, T. L. (2003). Patterns and causes of Atlanta's urban heat island–initiated  
504 precipitation. *Journal of Applied Meteorology*, 42(9), 1273-1284.  
505 [https://doi.org/10.1175/1520-0450\(2003\)042<1273:PACOAU>2.0.CO;2](https://doi.org/10.1175/1520-0450(2003)042<1273:PACOAU>2.0.CO;2)
- 506 Dudhia, J. (1989). Numerical study of convection observed during the winter monsoon  
507 experiment using a mesoscale two-dimensional model. *Journal of the Atmospheric  
508 Sciences*, 46(20), 3077-3107. [https://doi.org/10.1175/1520-0469\(1989\)046<3077:NSOCOD>2.0.CO;2](https://doi.org/10.1175/1520-0469(1989)046<3077:NSOCOD>2.0.CO;2)
- 510 Efstathiou, G., Zoumakis, N., Melas, D., Lolis, C., & Kassomenos, P. (2013). Sensitivity of  
511 WRF to boundary layer parameterizations in simulating a heavy rainfall event using  
512 different microphysical schemes. Effect on large-scale processes. *Atmospheric Research*,  
513 132, 125-143. <https://doi.org/10.1016/j.atmosres.2013.05.004>
- 514 Farley Nicholls, J., & Toumi, R. (2014). On the lake effects of the Caspian Sea. *Quarterly  
515 Journal of the Royal Meteorological Society*, 140(681), 1399-1408.  
516 <https://doi.org/10.1002/qj.2222>
- 517 Fernando, H. (2010). Fluid dynamics of urban atmospheres in complex terrain. *Annual review of  
518 fluid mechanics*, 42, 365-389. <https://doi.org/10.1146/annurev-fluid-121108-145459>
- 519 Freitag, B., Nair, U., & Niyogi, D. (2018). Urban modification of convection and rainfall in  
520 complex terrain. *Geophysical Research Letters*, 45(5), 2507-2515.  
521 <https://doi.org/10.1002/2017GL076834>
- 522 Gan, L., Guo, W., Deng, C., & Bureau, B. M. (2017). Comparative analysis of two torrential rain  
523 processes in Beijing. *Journal of Arid Meteorology*. (in Chinese)
- 524 Ganbat, G., Seo, J. M., Han, J.-Y., & Baik, J.-J. (2015). A theoretical study of the interactions of  
525 urban breeze circulation with mountain slope winds. *Theoretical and applied climatology*,  
526 121(3-4), 545-555. <https://doi.org/10.1007/s00704-014-1252-6>
- 527 Gu, H., Jin, J., Wu, Y., Ek, M. B., & Subin, Z. M. (2015). Calibration and validation of lake  
528 surface temperature simulations with the coupled WRF-lake model. *Climatic Change*,  
529 129(3-4), 471-483. <https://doi.org/10.1007/s10584-013-0978-y>
- 530 Gu, H., Ma, Z., & Li, M. (2016). Effect of a large and very shallow lake on local summer  
531 precipitation over the Lake Taihu basin in China. *Journal of Geophysical Research:  
532 Atmospheres*, 121(15), 8832-8848. <https://doi.org/10.1002/2015JD024098>

- 533 Hong, S.-Y., Dudhia, J., & Chen, S.-H. J. M. W. R. (2004). A revised approach to ice  
534 microphysical processes for the bulk parameterization of clouds and precipitation. 132(1),  
535 103-120. [https://doi.org/10.1175/1520-0493\(2004\)132<0103:ARATIM>2.0.CO;2](https://doi.org/10.1175/1520-0493(2004)132<0103:ARATIM>2.0.CO;2)
- 536 Janjić, Z. I. (1994). The step-mountain eta coordinate model: Further developments of the  
537 convection, viscous sublayer, and turbulence closure schemes. *Monthly Weather Review*,  
538 122(5), 927-945. [https://doi.org/10.1175/1520-493\(1994\)122<0927:TSMECM>2.0.CO;2](https://doi.org/10.1175/1520-493(1994)122<0927:TSMECM>2.0.CO;2)
- 539 Jin, M., & Dickinson, R. E. (2010). Land surface skin temperature climatology: benefitting from  
540 the strengths of satellite observations. *Environmental Research Letters*, 5(4), 044004.  
541 <https://doi.org/10.1088/1748-9326/5/4/044004>
- 542 Jin, M., Shepherd, J. M., & King, M. D. (2005). Urban aerosols and their variations with clouds  
543 and rainfall: a case study for New York and Houston. *Journal of Geophysical Research:*  
544 *Atmospheres*, 110(D10). <https://doi.org/10.1029/2004JD005081>
- 545 Laird, N., Sobash, R., & Hodas, N. (2009). The frequency and characteristics of lake-effect  
546 precipitation events associated with the New York State Finger Lakes. *Journal of Applied*  
547 *Meteorology and Climatology*, 48(4), 873-886. <https://doi.org/10.1175/2008JAMC2054.1>
- 548 Lin, C.-Y., Chen, F., Huang, J., Chen, W.-C., Liou, Y.-A., Chen, W.-N., & Liu, S.-C. (2008).  
549 Urban heat island effect and its impact on boundary layer development and land-sea  
550 circulation over northern Taiwan. *Atmospheric Environment*, 42(22), 5635-5649.  
551 <https://doi.org/10.1016/j.atmosenv.2008.03.015>
- 552 Lin, C.-Y., Chen, W.-C., Chang, P.-L., Sheng, Y.-F. (2011). Impact of the urban heat island  
553 effect on precipitation over a complex geographic environment in northern Taiwan.  
554 *Journal of Applied Meteorology*, 50(2), 339-353.  
555 <https://doi.org/10.1175/2010JAMC2504.1>
- 556 Liu, C., Ikeda, K., Thompson, G., Rasmussen, R., & Dudhia, J. (2011). High-resolution  
557 simulations of wintertime precipitation in the Colorado Headwaters region: Sensitivity to  
558 physics parameterizations. *Monthly Weather Review*, 139(11), 3533-3553.  
559 <https://doi.org/10.1175/MWR-D-11-00009.1>
- 560 Lo, J. C., Lau, A. K., Chen, F., Fung, J. C., & Leung, K. K. (2007). Urban modification in a  
561 mesoscale model and the effects on the local circulation in the Pearl River Delta region.  
562 *Journal of Applied Meteorology and Climatology*, 46(4), 457-476.  
563 <https://doi.org/10.1175/JAM2477.1>
- 564 Long, Z., Perrie, W., Gyakum, J., Caya, D., & Laprise, R. (2007). Northern lake impacts on local  
565 seasonal climate. *Journal of Hydrometeorology*, 8(4), 881-896.  
566 <https://doi.org/10.1175/JHM591.1>
- 567 Loose, T., & Bornstein, R. D. (1977). Observations of mesoscale effects on frontal movement  
568 through an urban area. *Monthly Weather Review*, 105(5), 563-571.  
569 [https://doi.org/10.1175/1520-0493\(1977\)105<0563:OOMEOF>2.0.CO;2](https://doi.org/10.1175/1520-0493(1977)105<0563:OOMEOF>2.0.CO;2)
- 570 McLeod, J., Shepherd, M., & Konrad II, C. E. (2017). Spatio-temporal rainfall patterns around  
571 Atlanta, Georgia and possible relationships to urban land cover. *Urban Climate*, 21, 27-  
572 42. <https://doi.org/10.1016/j.uclim.2017.03.004>

- 573 Miao, S., Chen, F., LeMone, M. A., Tewari, M., Li, Q., & Wang, Y. (2009). An observational  
574 and modeling study of characteristics of urban heat island and boundary layer structures  
575 in Beijing. *Journal of Applied Meteorology and Climatology*, 48(3), 484-501.  
576 <https://doi.org/10.1175/2008JAMC1909.1>
- 577 Miao, S., Chen, F., Li, Q., & Fan, S. (2011). Impacts of urban processes and urbanization on  
578 summer precipitation: A case study of heavy rainfall in Beijing on 1 August 2006.  
579 *Journal of Applied Meteorology and Climatology*, 50(4), 806-825.  
580 <https://doi.org/10.1175/2010JAMC2513.1>
- 581 Mlawer, E. J., Taubman, S. J., Brown, P. D., Iacono, M. J., & Clough, S. A. (1997). Radiative  
582 transfer for inhomogeneous atmospheres: RRTM, a validated correlated-k model for the  
583 longwave. *Journal of Geophysical Research: Atmospheres*, 102(D14), 16663-16682.  
584 <https://doi.org/10.1029/97JD00237>
- 585 Monin, A. S., & Obukhov, A. M. (1954). Basic laws of turbulent mixing in the surface layer of  
586 the atmosphere. *Contrib. Geophys. Inst. Acad. Sci. USSR*, 151(163), e187.
- 587 Nie, W., Zaitchik, B. F., Ni, G., & Sun, T. (2017). Impacts of anthropogenic heat on summertime  
588 rainfall in Beijing. *Journal of Hydrometeorology*, 18(3), 693-712.  
589 <https://doi.org/10.1175/JHM-D-16-0173.1>
- 590 Niyogi, D., Pyle, P., Lei, M., Arya, S. P., Kishtawal, C. M., Shepherd, M., et al. (2011). Urban  
591 modification of thunderstorms: An observational storm climatology and model case study  
592 for the Indianapolis urban region. *Journal of Applied Meteorology and Climatology*,  
593 50(5), 1129-1144. <https://doi.org/10.1175/2010JAMC1836.1>
- 594 Notaro, M., Holman, K., Zarrin, A., Fluck, E., Vavrus, S., & Bennington, V. (2013). Influence of  
595 the Laurentian Great Lakes on regional climate. *Journal of Climate*, 26(3), 789-804.  
596 <https://doi.org/10.1175/JCLI-D-12-00140.1>
- 597 Ntelekos, A. A., Smith, J. A., Donner, L., Fast, J. D., Gustafson Jr, W. I., Chapman, E. G., &  
598 Krajewski, W. F. (2009). The effects of aerosols on intense convective precipitation in  
599 the northeastern United States. *Quarterly Journal of the Royal Meteorological Society: A*  
600 *journal of the atmospheric sciences, applied meteorology and physical oceanography*,  
601 135(643), 1367-1391. <https://doi.org/10.1002/qj.476>
- 602 Ohashi, Y., & Kida, H. (2002). Local circulations developed in the vicinity of both coastal and  
603 inland urban areas: A numerical study with a mesoscale atmospheric model. *Journal of*  
604 *Applied Meteorology*, 41(1), 30-45. [https://doi.org/10.1175/1520-0450\(2002\)041<0030:LCDITV>2.0.CO;2](https://doi.org/10.1175/1520-0450(2002)041<0030:LCDITV>2.0.CO;2)
- 606 Paul, S., Ghosh, S., Mathew, M., Devanand, A., Karmakar, S., & Niyogi, D. (2018). Increased  
607 spatial variability and intensification of extreme monsoon rainfall due to Urbanization.  
608 *Scientific reports*, 8(1), 3918. <https://doi.org/10.1038/s41598-018-22322-9>
- 609 Qiao, Z., Wu, C., Zhao, D., Xu, X., Yang, J., Feng, L., et al. (2019). Determining the Boundary  
610 and Probability of Surface Urban Heat Island Footprint Based on a Logistic Model.  
611 *Remote Sensing*, 11(11), 1368. <https://doi.org/10.3390/rs11111368>
- 612 Reames, L. J., & Stensrud, D. J. (2018). Influence of a Great Plains urban environment on a  
613 simulated supercell. *Monthly Weather Review*, 146(5), 1437-1462.  
614 <https://doi.org/10.1175/MWR-D-17-0284.1>

- 615 Ryu, Y.-H., Smith, J. A., Bou-Zeid, E., & Baeck, M. L. (2016). The influence of land surface  
616 heterogeneities on heavy convective rainfall in the Baltimore–Washington metropolitan  
617 area. *Monthly Weather Review*, 144(2), 553-573. [https://doi.org/10.1175/MWR-D-15-](https://doi.org/10.1175/MWR-D-15-0192.1)  
618 [0192.1](https://doi.org/10.1175/MWR-D-15-0192.1)
- 619 Shem, W., & Shepherd, M. (2009). On the impact of urbanization on summertime thunderstorms  
620 in Atlanta: Two numerical model case studies. *Atmospheric Research*, 92(2), 172-189.  
621 <https://doi.org/10.1016/j.atmosres.2008.09.013>
- 622 Shepherd, J. M. (2005). A review of current investigations of urban-induced rainfall and  
623 recommendations for the future. *Earth Interactions*, 9(12), 1-27.  
624 <https://doi.org/10.1175/EI156.1>
- 625 Shepherd, J. M., & Burian, S. J. (2003). Detection of urban-induced rainfall anomalies in a major  
626 coastal city. *Earth Interactions*, 7(4), 1-17. [https://doi.org/10.1175/1087-](https://doi.org/10.1175/1087-3562(2003)007<0001:DOUIRA>2.0.CO;2)  
627 [3562\(2003\)007<0001:DOUIRA>2.0.CO;2](https://doi.org/10.1175/1087-3562(2003)007<0001:DOUIRA>2.0.CO;2)
- 628 Shepherd, J. M., Carter, M., Manyin, M., Messen, D., & Burian, S. (2010). The impact of  
629 urbanization on current and future coastal precipitation: a case study for Houston.  
630 *Environment and Planning B: Planning and Design*, 37(2), 284-304.  
631 <https://doi.org/10.1068/b34102t>
- 632 Shepherd, J. M., Pierce, H., & Negri, A. J. (2002). Rainfall modification by major urban areas:  
633 Observations from spaceborne rain radar on the TRMM satellite. *Journal of Applied*  
634 *Meteorology*, 41(7), 689-701. [https://doi.org/10.1175/1520-](https://doi.org/10.1175/1520-0450(2002)041<0689:RMBMUA>2.0.CO;2)  
635 [0450\(2002\)041<0689:RMBMUA>2.0.CO;2](https://doi.org/10.1175/1520-0450(2002)041<0689:RMBMUA>2.0.CO;2)
- 636 Singh, J., Vittal, H., Karmakar, S., Ghosh, S., & Niyogi, D. (2016). Urbanization causes  
637 nonstationarity in Indian summer monsoon rainfall extremes. *Geophysical Research*  
638 *Letters*, 43(21). <https://doi.org/10.1002/2016GL071238>
- 639 Singh, K., Bonthu, S., Purvaja, R., Robin, R., Kannan, B., & Ramesh, R. (2018). Prediction of  
640 heavy rainfall over Chennai Metropolitan City, Tamil Nadu, India: impact of  
641 microphysical parameterization schemes. *Atmospheric Research*, 202, 219-234.  
642 <https://doi.org/10.1016/j.atmosres.2017.11.028>
- 643 Skamarock, W., Klemp, J., Dudhia, J., Gill, D., Barker, D., Duda, M., et al. (2008). A description  
644 of the advanced research WRF Version 3, NCAR technical note, Mesoscale and  
645 Microscale Meteorology Division. National Center for Atmospheric Research, Boulder,  
646 Colorado, USA.
- 647 Souma, K., Tanaka, K., Suetsugi, T., Sunada, K., Tsuboki, K., Shinoda, T., et al. (2013). A  
648 comparison between the effects of artificial land cover and anthropogenic heat on a  
649 localized heavy rain event in 2008 in Zoshigaya, Tokyo, Japan. *Journal of Geophysical*  
650 *Research: Atmospheres*, 118(20), 11,600-611,610. <https://doi.org/10.1002/jgrd.50850>
- 651 Sousounis, P. J., & Mann, G. E. (2000). Lake-aggregate mesoscale disturbances. Part V: Impacts  
652 on lake-effect precipitation. *Monthly Weather Review*, 128(3), 728-745.  
653 [https://doi.org/10.1175/1520-0493\(2000\)128<0728:LAMDPV>2.0.CO;2](https://doi.org/10.1175/1520-0493(2000)128<0728:LAMDPV>2.0.CO;2)
- 654 Stensrud, D. J. (2009). *Parameterization schemes: keys to understanding numerical weather*  
655 *prediction models*: Cambridge University Press, Cambridge.

- 656 Stivari, S. M., de Oliveira, A. P., Karam, H. A., & Soares, J. (2003). Patterns of local circulation  
657 in the Itaipu Lake area: numerical simulations of lake breeze. *Journal of Applied*  
658 *Meteorology*, 42(1), 37-50. [https://doi.org/10.1175/1520-](https://doi.org/10.1175/1520-0450(2003)042<0037:POLCIT>2.0.CO;2)  
659 [0450\(2003\)042<0037:POLCIT>2.0.CO;2](https://doi.org/10.1175/1520-0450(2003)042<0037:POLCIT>2.0.CO;2)
- 660 Subin, Z. M., Riley, W. J., & Mironov, D. (2012). An improved lake model for climate  
661 simulations: model structure, evaluation, and sensitivity analyses in CESM1. *Journal of*  
662 *Advances in Modeling Earth Systems*, 4(1). <https://doi.org/10.1029/2011MS000072>
- 663 Sun, X., Xie, L., Semazzi, F., & Liu, B. (2015). Effect of lake surface temperature on the spatial  
664 distribution and intensity of the precipitation over the Lake Victoria basin. *Monthly*  
665 *Weather Review*, 143(4), 1179-1192. <https://doi.org/10.1175/MWR-D-14-00049.1>
- 666 Theeuwes, N., Solcerová, A., & Steeneveld, G. (2013). Modeling the influence of open water  
667 surfaces on the summertime temperature and thermal comfort in the city. *Journal of*  
668 *Geophysical Research: Atmospheres*, 118(16), 8881-8896.  
669 <https://doi.org/10.1002/jgrd.50704>
- 670 Wilson, J. W. (1977). Effect of Lake Ontario on precipitation. *Monthly Weather Review*, 105(2),  
671 207-214. [https://doi.org/10.1175/1520-0493\(1977\)105<0207:EOLoop>2.0.CO;2](https://doi.org/10.1175/1520-0493(1977)105<0207:EOLoop>2.0.CO;2)
- 672 Yang, L., Smith, J. A., Baek, M. L., Bou-Zeid, E., Jessup, S. M., Tian, F., & Hu, H. (2014a).  
673 Impact of urbanization on heavy convective precipitation under strong large-scale  
674 forcing: A case study over the Milwaukee–Lake Michigan region. *Journal of*  
675 *Hydrometeorology*, 15(1), 261-278. <https://doi.org/10.1175/JHM-D-13-020.1>
- 676 Yang, L., Tian, F., Smith, J. A., & Hu, H. (2014b). Urban signatures in the spatial clustering of  
677 summer heavy rainfall events over the Beijing metropolitan region. *Journal of*  
678 *Geophysical Research: Atmospheres*, 119(3), 1203-1217.  
679 <https://doi.org/10.1002/2013JD020762>
- 680 Yeung, J. K., Smith, J. A., Baek, M. L., & Villarini, G. (2015). Lagrangian analyses of rainfall  
681 structure and evolution for organized thunderstorm systems in the urban corridor of the  
682 northeastern United States. *Journal of Hydrometeorology*, 16(4), 1575-1595.  
683 <https://doi.org/10.1175/JHM-D-14-0095.1>
- 684 Zhang, W., Villarini, G., Vecchi, G. A., & Smith, J. A. (2018). Urbanization exacerbated the  
685 rainfall and flooding caused by hurricane Harvey in Houston. *Nature*, 563(7731), 384.  
686 <https://doi.org/10.1038/s41586-018-0676-z>
- 687 Zhang, Y., Miao, S., Dai, Y., & Bornstein, R. (2017). Numerical simulation of urban land  
688 surface effects on summer convective rainfall under different UHI intensity in Beijing.  
689 *Journal of Geophysical Research: Atmospheres*, 122(15), 7851-7868.  
690 <https://doi.org/10.1002/2017JD026614>  
691

## 692 List of Tables

693 **Table 1.** Overview of WRF physics options.

Physics	Scheme	Reference
Microphysics	WSM5	Hong et al. (2004)
PBL	MYJ	Janjić (1994)
Shortwave radiation	Dudhia	Dudhia (1989)
Longwave radiation	RRTM	Mlawer et al. (1997)
Land surface scheme	Noah LSM	Chen & Dudhia (2001)
Surface layer scheme	Monin-Obukhov	Monin & Obukhov (1954)
Cumulus	None	None
Surface urban physics	UCM	Chen et al. (2011)
Surface lake physics	LAKE	Gu et al. (2015)

694 **Table 2.** Lake and urban areas in six WRF simulations.

Scenario	Lake Area (km <sup>2</sup> )	Urban Area (km <sup>2</sup> )
CTRL	281	0
URB	0	1417
BASE	0	0
ULS	281	120
ULM	281	410
ULL	281	1136

695 **Table 3.** Statistics of the CTRL simulation results for 2-m temperature, 2-m relative humidity,  
696 hourly rain rate, and 10-m wind speed.

	Mean Bias	RMSE	Correlation	HR
T2 (°C)	-0.84	1.82	0.73	0.96
RH2 (%)	-2.08	6.48	0.70	0.81
Rain rate (mm)	0.06	4.67	0.58	0.92
UV10 (m s <sup>-1</sup> )	1.76	2.99	0.78	0.62

697 Note. The statistics are averaged between 16 UTC18 July and 00 UTC 22 July over the 30 in-situ  
698 weather stations and corresponding model grids. The thresholds used for calculating the hit rate  
699 (HR) are 2 °C for T2, 2 % for RH2, 2 mm for Rain rate, and 2 m s<sup>-1</sup> for UV10.

700 List of Figures

701 **Figure 1.** (a) Three nested domains used for the numerical simulations with elevation shaded in  
 702 color. (b) spatial extent of domain 3 (with elevation shaded in color). The red polygon represents  
 703 the urban boundary (for the ULL scenario), and the green polygon represents the Baiyang Lake.  
 704 Black circles in (b) denote surface weather stations and the star represents the radiosonde station.  
 705 The dashed black box outlines the projection of maximum development for XNA.

706 **Figure 2.** Land use/land cover for six different numerical experiments. (a) CTRL, (b) URB, (c)  
 707 BASE, (d) ULS, (e) ULM, and (f) ULL. The dashed box outlines the projection of maximum  
 708 development for XNA.

709 **Figure 3.** Geopotential height (with contour at every 10 gpm) at 500 hPa, wind fields (vector, in  
 710  $\text{m s}^{-1}$ ) at 500 hPa and IVT (shade, in  $\text{kg m}^{-1} \text{s}^{-1}$ ) based on the FNL reanalysis fields for (a) 18  
 711 UTC 18 July, (b) 12 UTC 19 July, (c) 06 UTC 20 July and (d) 00 UTC 21 July 2016. The red  
 712 rectangle outlines the innermost domain.

713 **Figure 4.** Time series of simulated and observed (a) 2-m temperature ( $T_2$ ,  $^{\circ}\text{C}$ ), (b) 2-m relative  
 714 humidity ( $\text{RH}_2$ , %), (c) 10-m wind speed ( $\text{UV}_{10}$ ,  $\text{m s}^{-1}$ ), and (d) rain rate ( $\text{mm h}^{-1}$ ). Blue (red)  
 715 lines indicate the median values of all the weather stations (corresponding model grids in the  
 716 CTRL simulation). Shades represent the inter-quartile ranges.

717 **Figure 5.** Hourly rain rates ( $\text{mm h}^{-1}$ ) at (a) (d) 22 UTC 19 July, (b) (e) 00 UTC 20 July, and (c)  
 718 (f) 02 UTC 20 July 2016 from the CMORPH rainfall product (upper panel), and the CTRL  
 719 simulation (lower panel). The CTRL simulation shows results from domain 3. Scatters represent  
 720 gauge-based observations.

721 **Figure 6.** Vertical profiles of (a, d) temperature (in  $^{\circ}\text{C}$ ), (b, e) water vapor mixing ratio (in  $\text{g kg}^{-1}$ ),  
 722 and wind speed (in  $\text{m s}^{-1}$ ) at the radiosonde station and the corresponding model grid. (a-c) 12  
 723 UTC 19 July, (b-f) 00 UTC 20 July.

724 **Figure 7.** Time series of hourly rain rates averaged over XNA region (the black dashed box  
 725 shown in Figure 1) for (a) BASE, CTRL and URB, (b) CTRL, ULS, ULM, and ULL. (c) shows  
 726 differences in rainfall accumulation between CTRL, URB, ULS, ULM, ULL and BASE. The  
 727 dashed lines in (a) and (b) indicate the dividing moment between the two storm episodes.

728 **Figure 8.** Differences of rainfall accumulation (in mm) for the first (upper panel) and second  
 729 storm episode (lower panel) between (a, c) CTRL and BASE, (b, d) URB and BASE. Vectors  
 730 represent wind fields of 500 hPa at 16 UTC 18 July and 17 UTC 19 July in CTRL and URB. The  
 731 red polygon represents the extent of urban coverage. The green polygon represents the lake. The  
 732 blue dashed lines highlight the location of cross sections used for the following analyses.

733 **Figure 9.** Differences of 2-m temperature ( $T_2$ , shade, in K), 2-m specific humidity ( $Q_2$ , contour  
 734 at every  $0.5 \text{ g kg}^{-1}$ ) and 10-m wind speed ( $\text{UV}_{10}$ , shade, in  $\text{m s}^{-1}$ ) (a, b, e, f) before the first storm  
 735 episode (averaged during 17 UTC to 19 UTC 18 July) and (c, d, g, h) before the second storm  
 736 episode (averaged during 12 UTC to 14 UTC 19 July) between CTRL, URB and BASE.

737 **Figure 10.** Cross sections of vertical velocity (shaded,  $\text{m s}^{-1}$ ) and wind field profile (vectors,  $\text{m s}^{-1}$ )  
 738 along line AB (shown in Figure 8) before the first storm episode (17 UTC 18 July, upper  
 739 panel) and line CD before the second storm episode (14 UTC 19 July, lower panel) of BASE,

740 CTRL and URB. The blue horizontal solid lines represent the lake while the red horizontal solid  
741 lines represent the urban extent.

742 **Figure 11.** Time series of moisture budget components averaged over XNA (the black dashed  
743 box shown in Figure 1) for (a) CTRL, (b) URB, (c) BASE, (d) ULS, (e) ULM, and (f) ULL. Rain  
744 rate ( $\text{mm h}^{-1}$ ), evaporation ( $\text{mm h}^{-1}$ ), precipitable water (mm) and convergence of water vapor  
745 ( $\text{mm h}^{-1}$ ) are represented by black, red, blue, and green curves, respectively. The dashed lines  
746 indicate the dividing moment between the two storm episodes.

747 **Figure 12.** Differences of rainfall accumulation (in mm) for the first (upper panel) and second  
748 storm episode (lower panel) between (a-g) three urban simulations and the CTRL simulation, (d,  
749 h) the ULL and URB simulation. Vectors represent wind fields of 500 hPa at 16 UTC 18 July  
750 and 17 UTC 19 July in ULS, ULM and ULL simulations. The red polygons represent the extent  
751 of urban coverage. The green polygons represent the Lake. The blue dashed lines highlight the  
752 location of cross sections used for the following analyses.

753 **Figure 13.** Differences of 2-m temperature ( $T_2$ , shade, in K), 2-m specific humidity ( $Q_2$ , contour  
754 at every  $0.5 \text{ g kg}^{-1}$ ) and 10-m wind speed ( $UV_{10}$ , shade, in  $\text{m s}^{-1}$ ) (a-c, g-i) before the first storm  
755 episode (averaged during 17 UTC to 19 UTC 18 July) and (d-f, j-l) before the second storm  
756 episode (averaged during 12 UTC to 14 UTC 19 July) between ULS, ULM, ULL and CTRL.

757 **Figure 14.** Lifted Index before (a-f) the first storm episode and (g-l) the second storm episode  
758 for the six scenarios.

759 **Figure 15.** Cross sections of CAPE (shaded,  $\text{J kg}^{-1}$ ) and CIN (contour at every  $10 \text{ J kg}^{-1}$ ) along  
760 line AB at 20 UTC 18 July (left column) and line CD at 12 UTC 19 July (right column) of  
761 CTRL, ULS, ULM, and ULL. The solid black horizontal lines represent the urban area in the  
762 three simulations.

763 **Figure 16.** Cross sections of vertical velocity (shaded, in  $\text{m s}^{-1}$ ) and mixing ratio (contour at  
764 every  $2 \text{ g kg}^{-1}$ ) along line AB averaged from 20 UTC to 23 UTC 18 July (left column) and line  
765 CD averaged from 14 UTC to 17 UTC 19 July (right column). The solid black horizontal lines  
766 represent the urban area in the four simulations.

Figure 1.

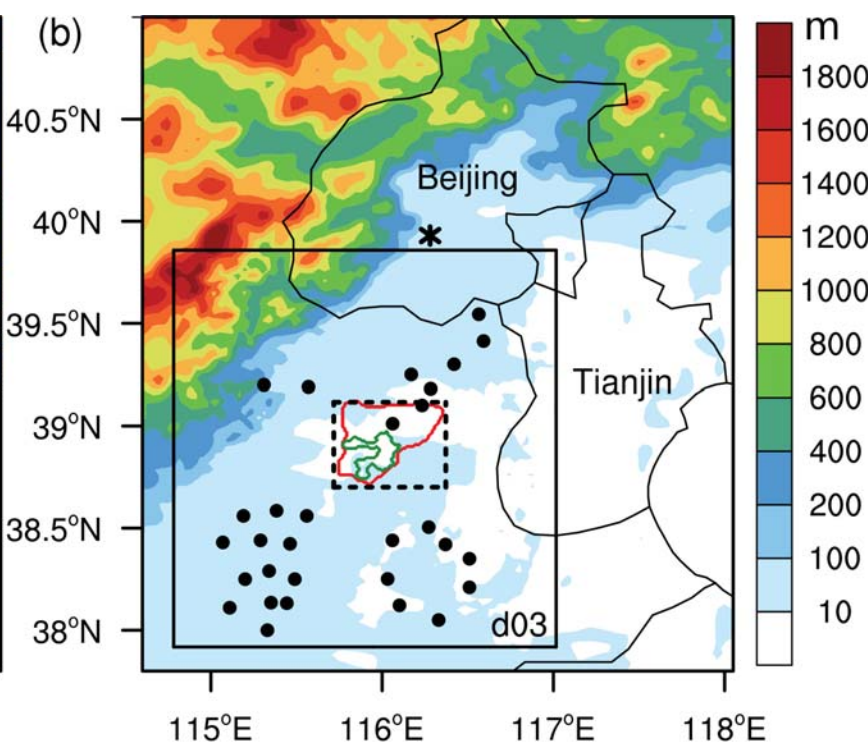
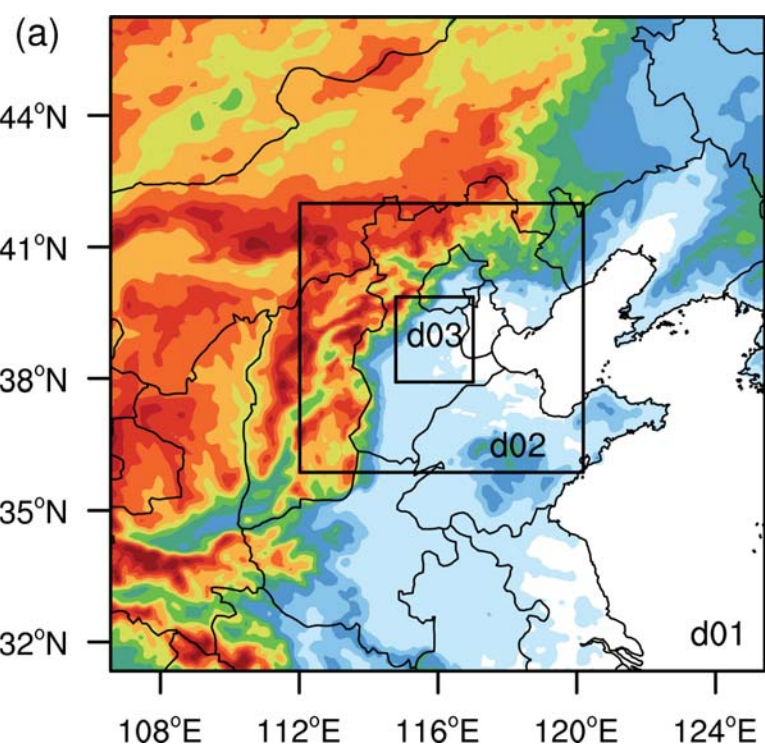
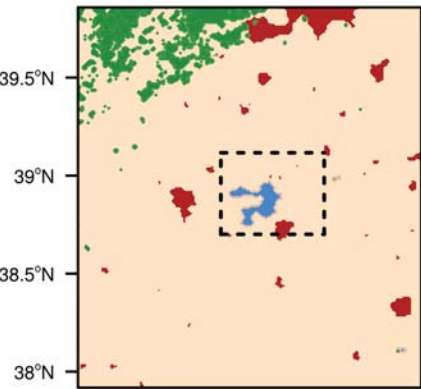
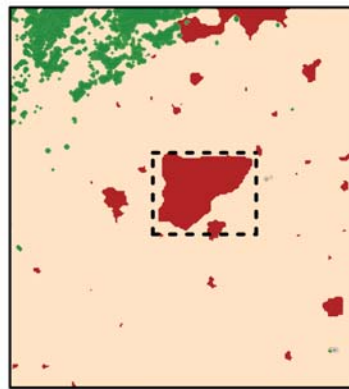


Figure 2.

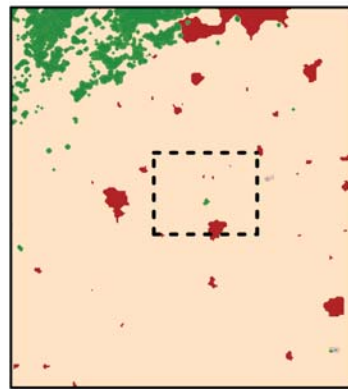
(a) CTRL



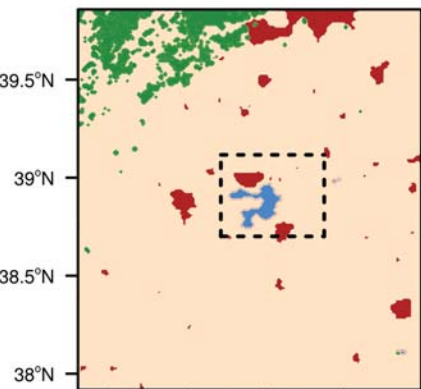
(b) URB



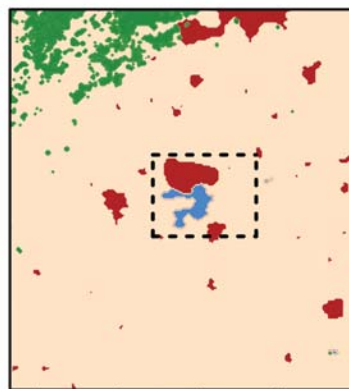
(c) BASE



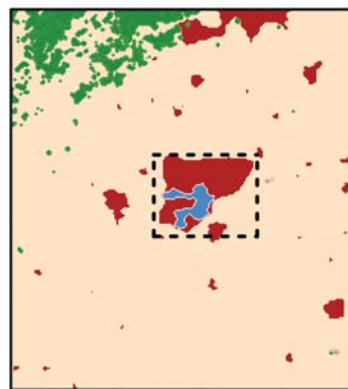
(d) ULS



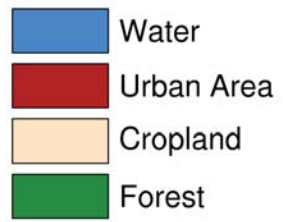
(e) ULM



(f) ULL



Main Land Use Types



115°E 115.5°E 116°E 116.5°E

115°E 115.5°E 116°E 116.5°E

115°E 115.5°E 116°E 116.5°E

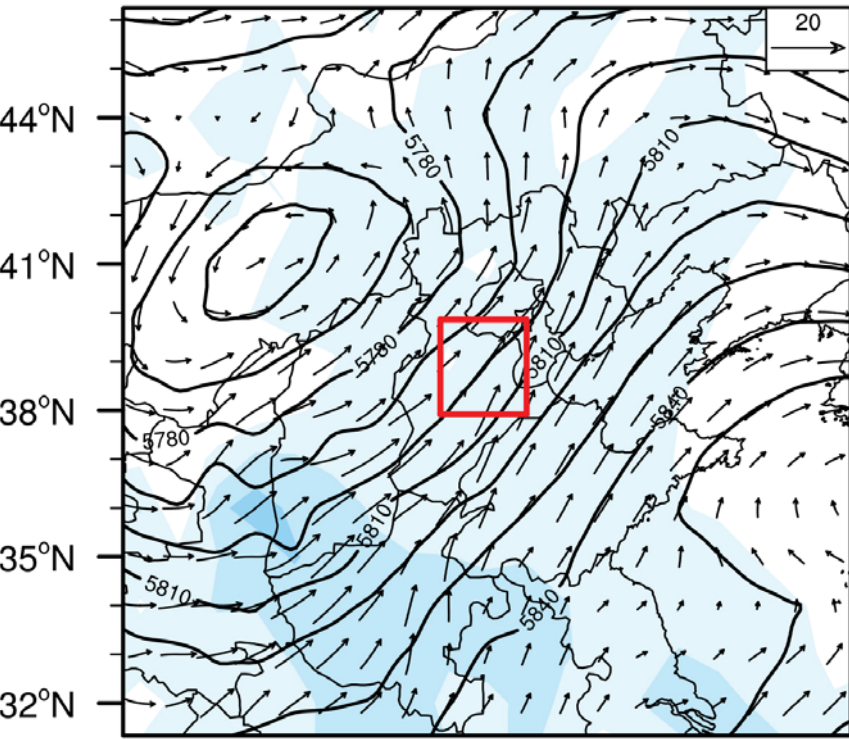
39.5°N  
39°N  
38.5°N  
38°N

39.5°N  
39°N  
38.5°N  
38°N

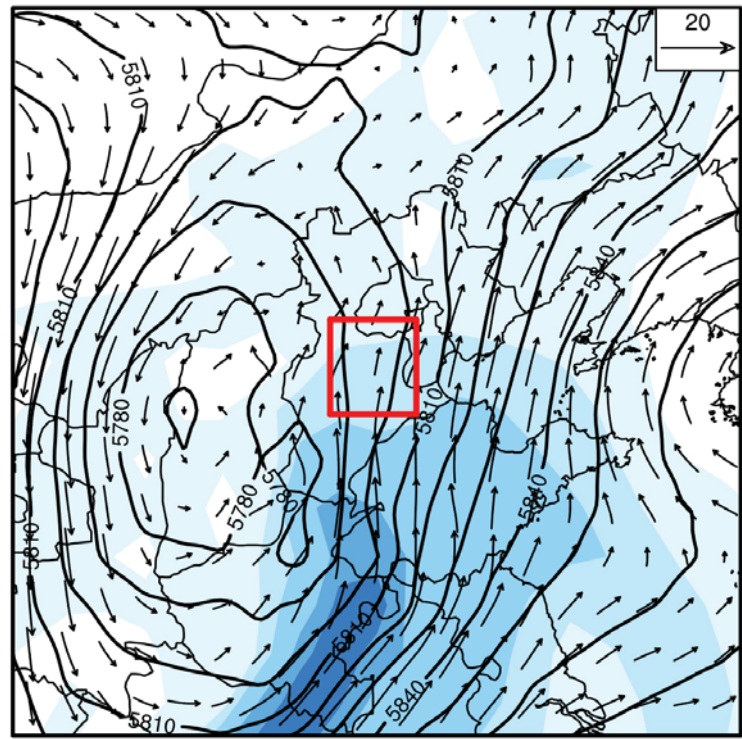
39.5°N  
39°N  
38.5°N  
38°N

Figure 3.

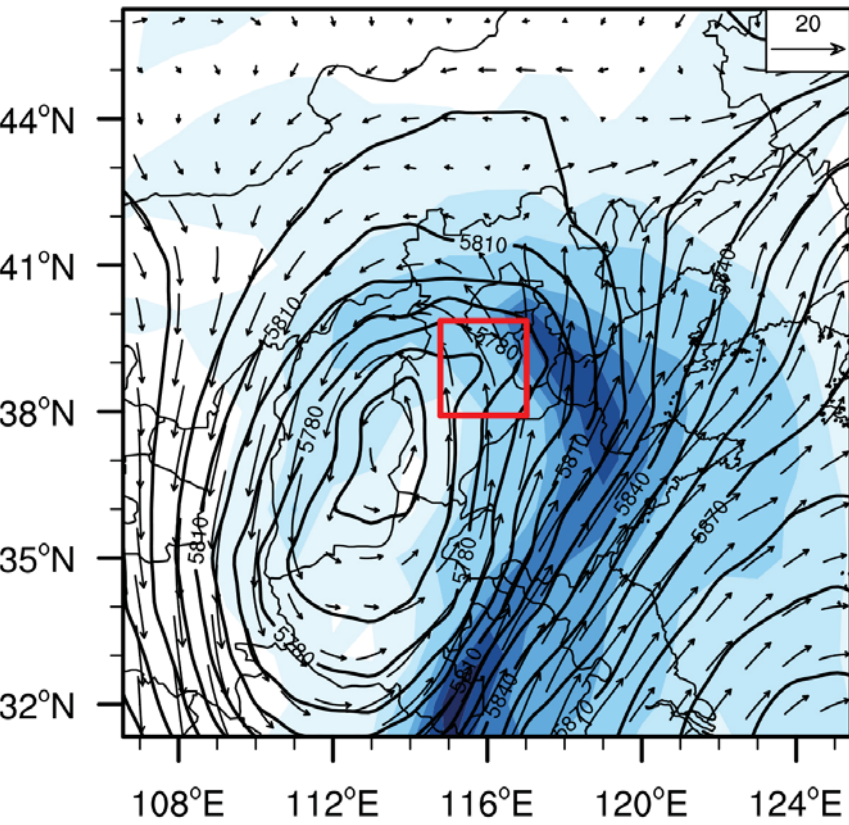
(a) 18 UTC 18 July



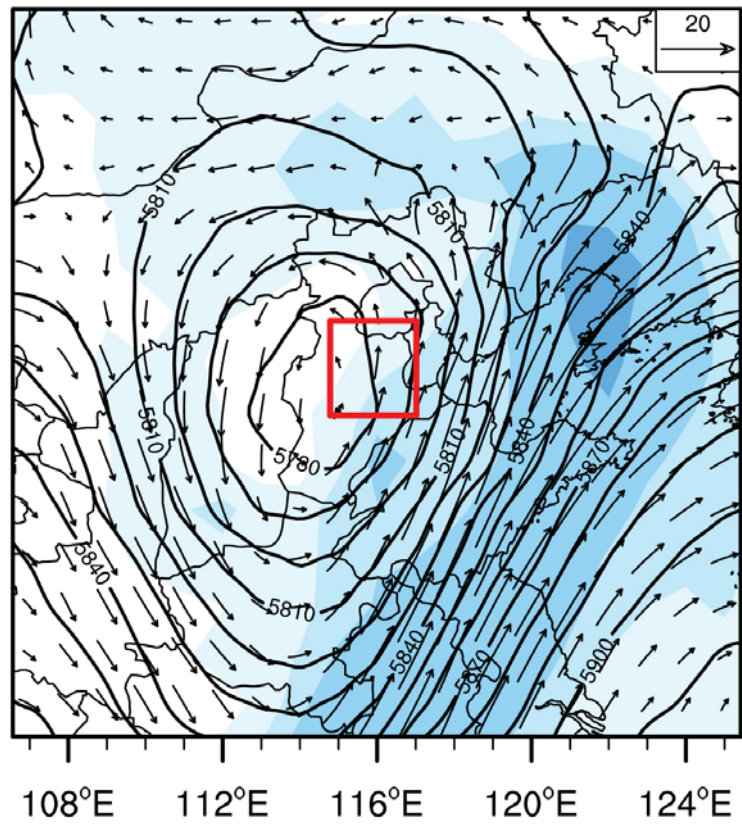
(b) 12 UTC 19 July



(c) 06 UTC 20 July



(d) 00 UTC 21 July



IVT ( $\text{kg m}^{-1} \text{s}^{-1}$ )

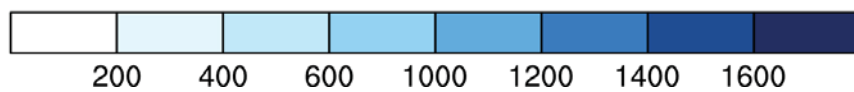


Figure 4.

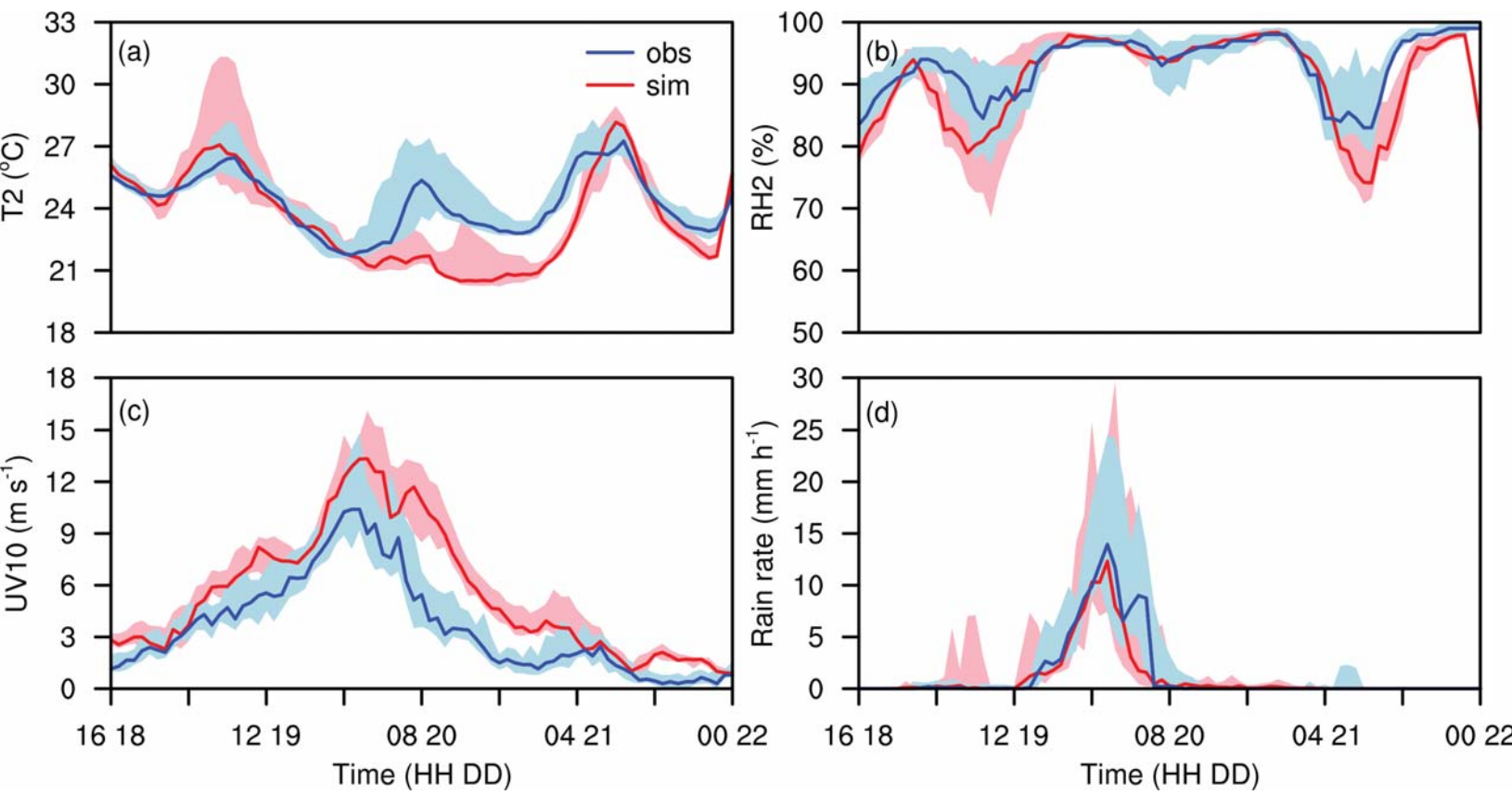


Figure 5.

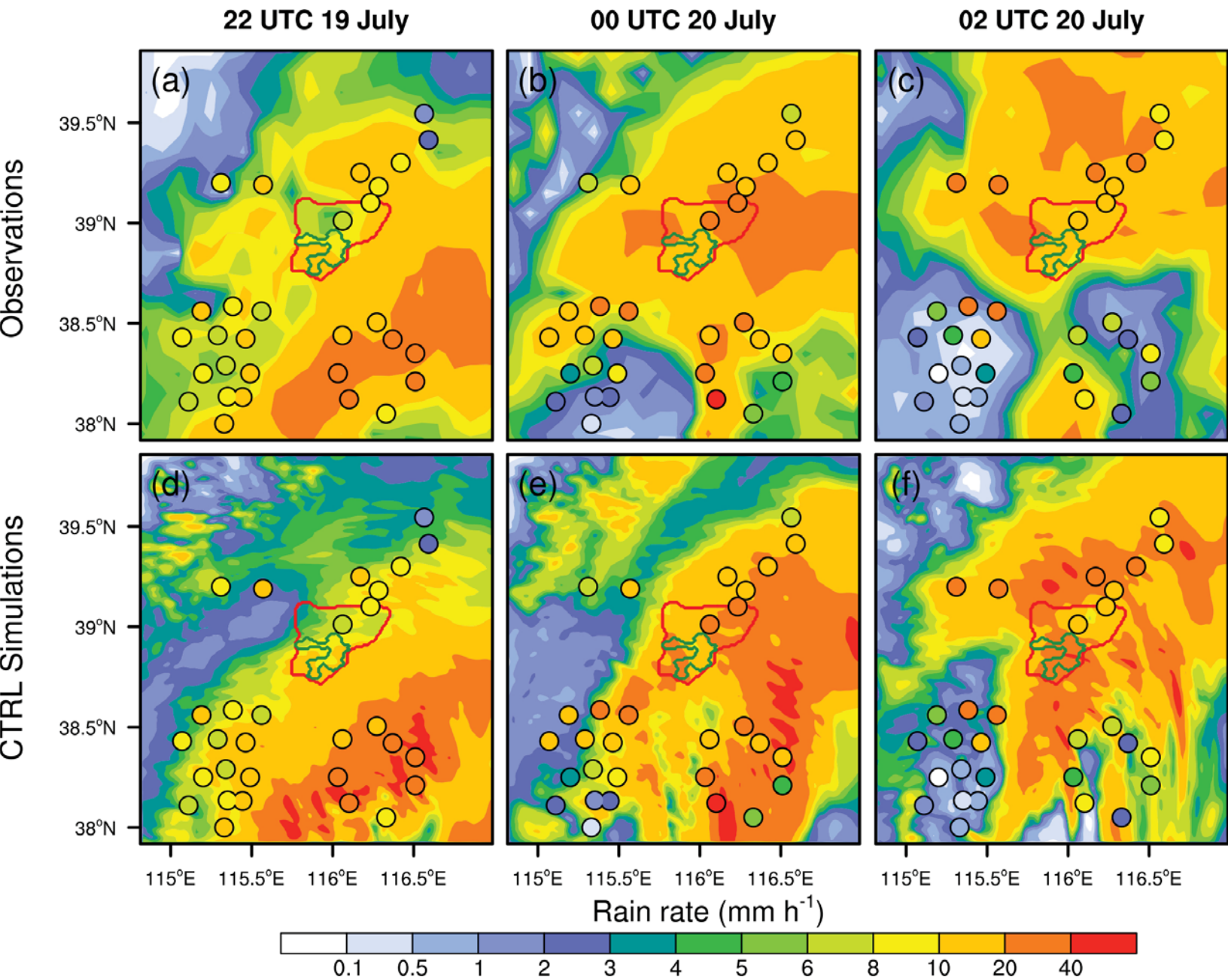
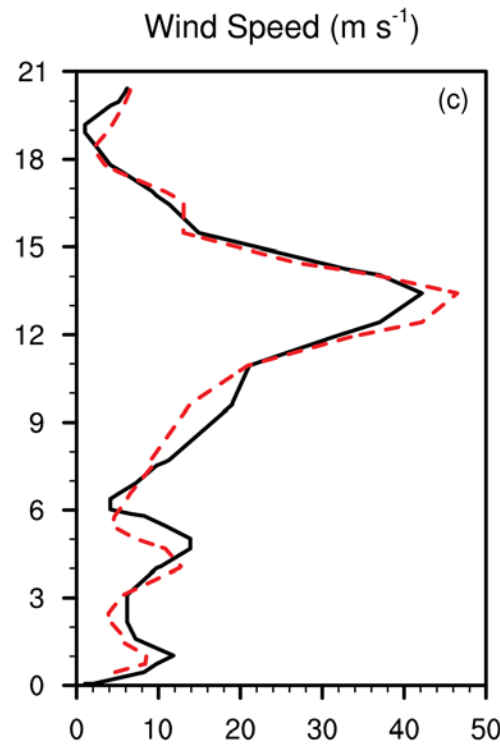
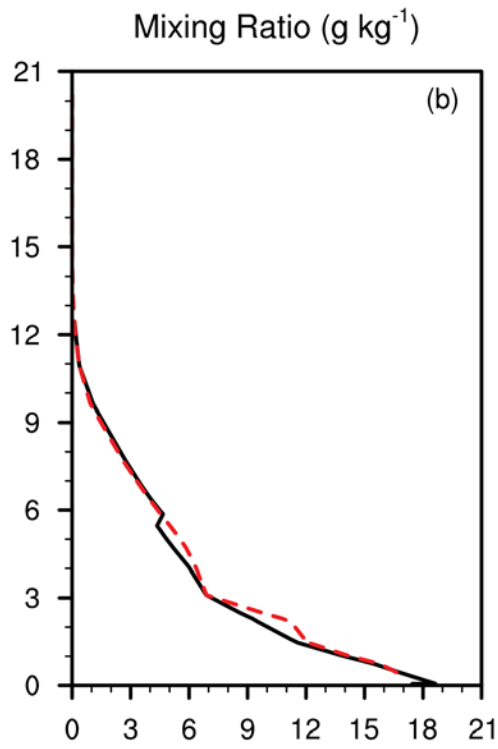
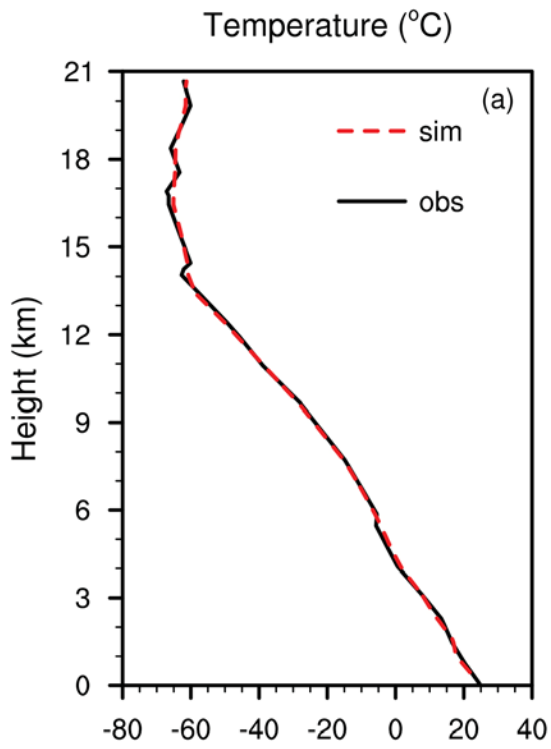
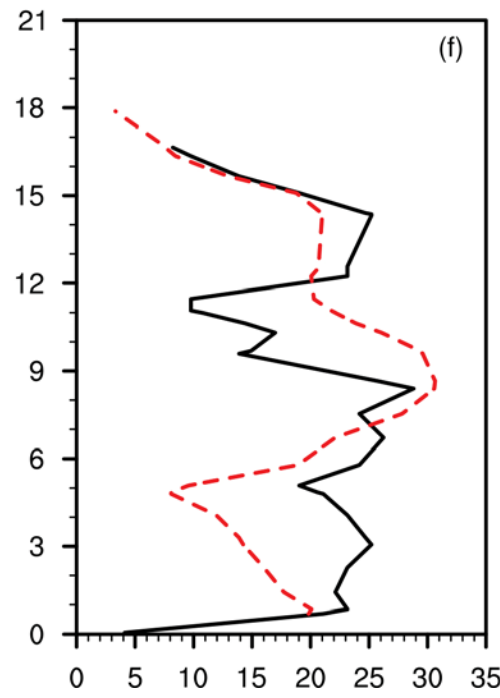
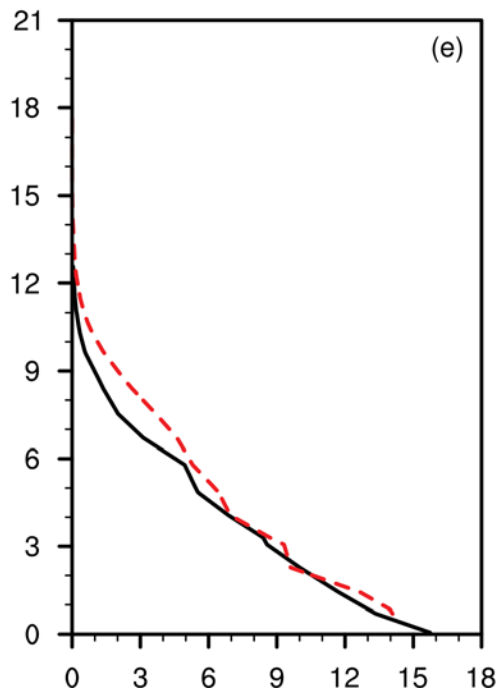
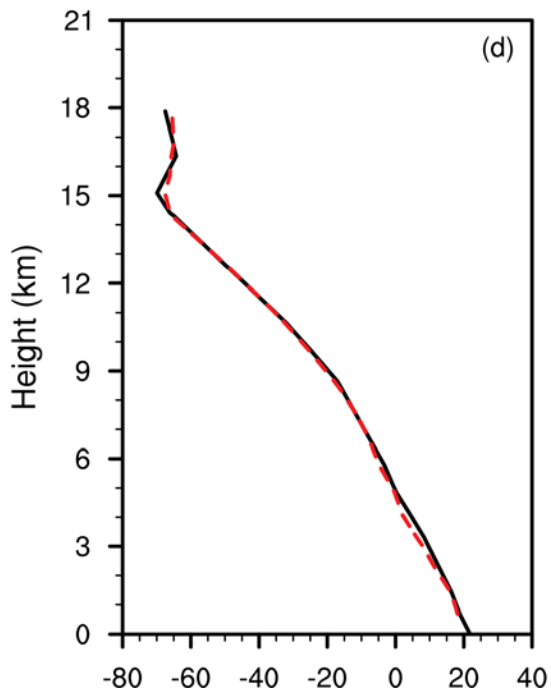


Figure 6.

12 OCT 19 July



00 OCT 20 July



**Figure 7.**

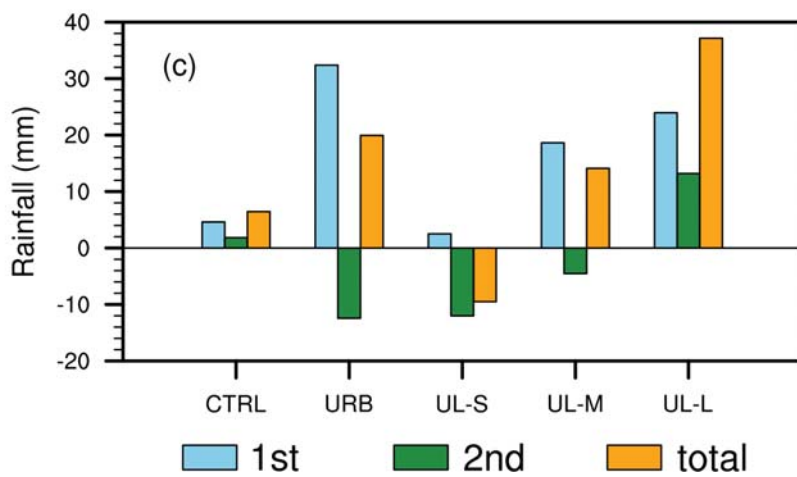
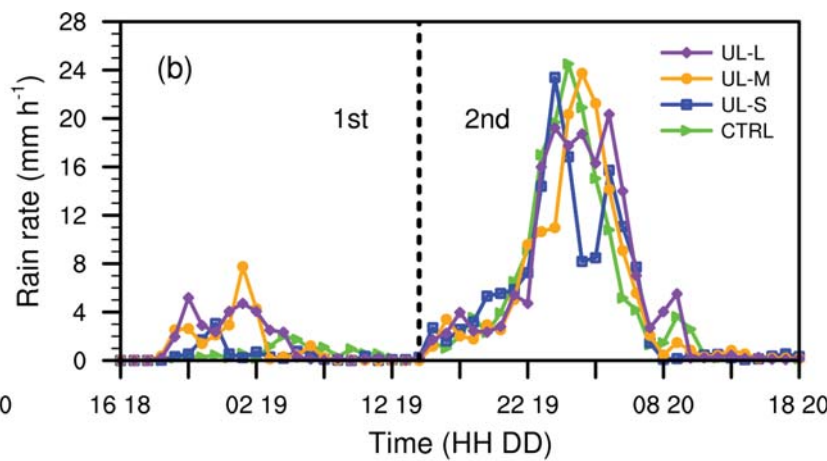
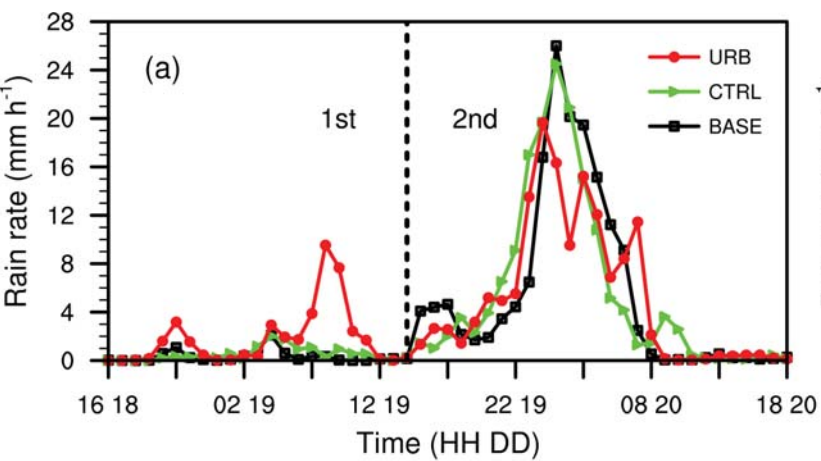
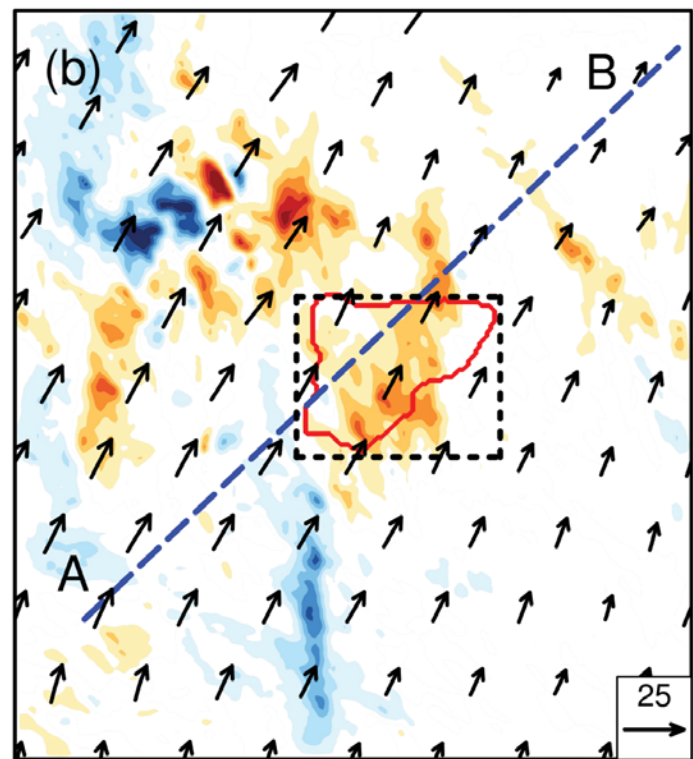
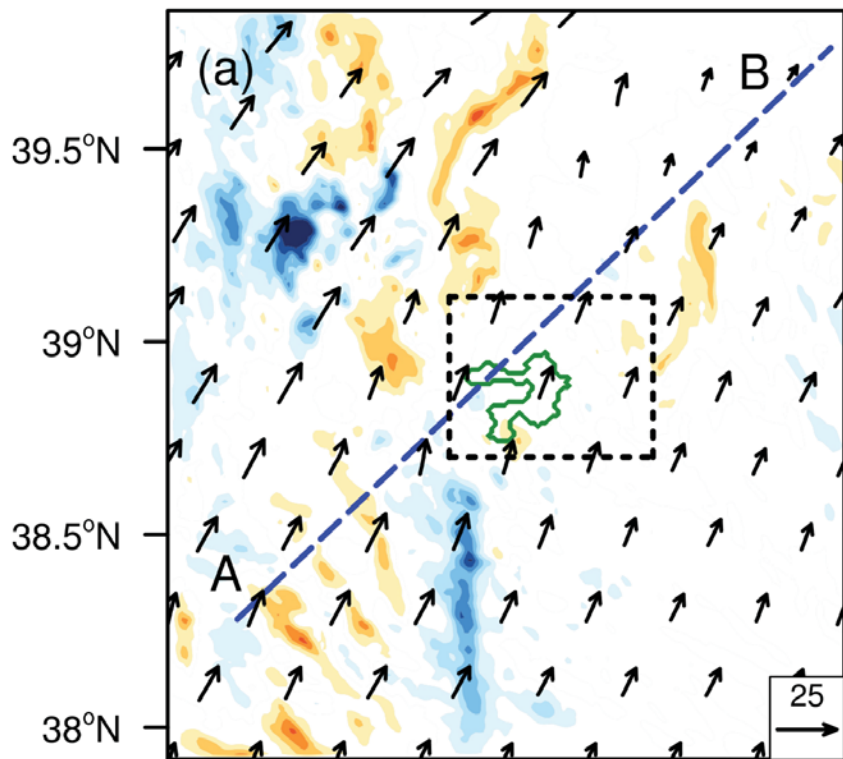


Figure 8.

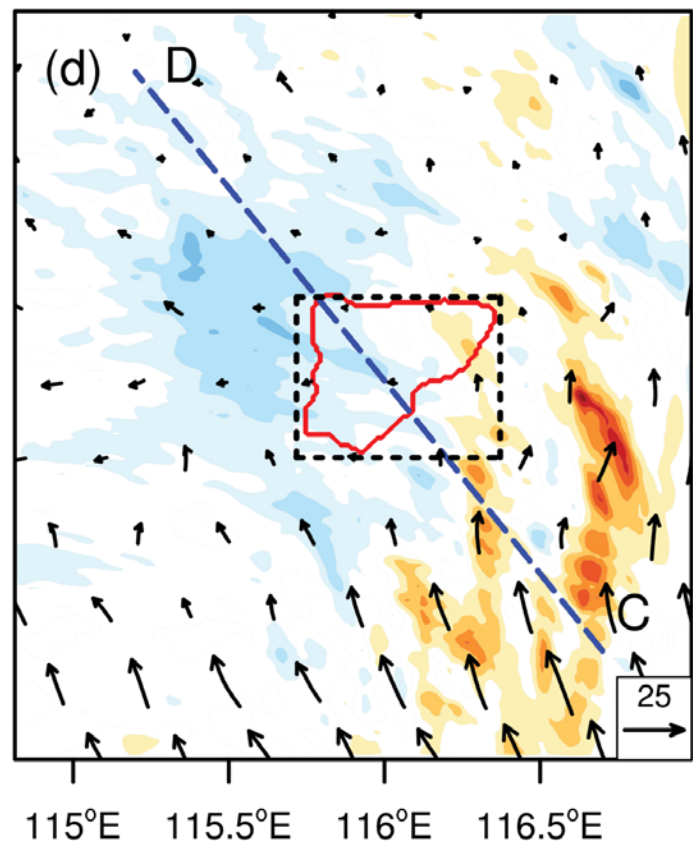
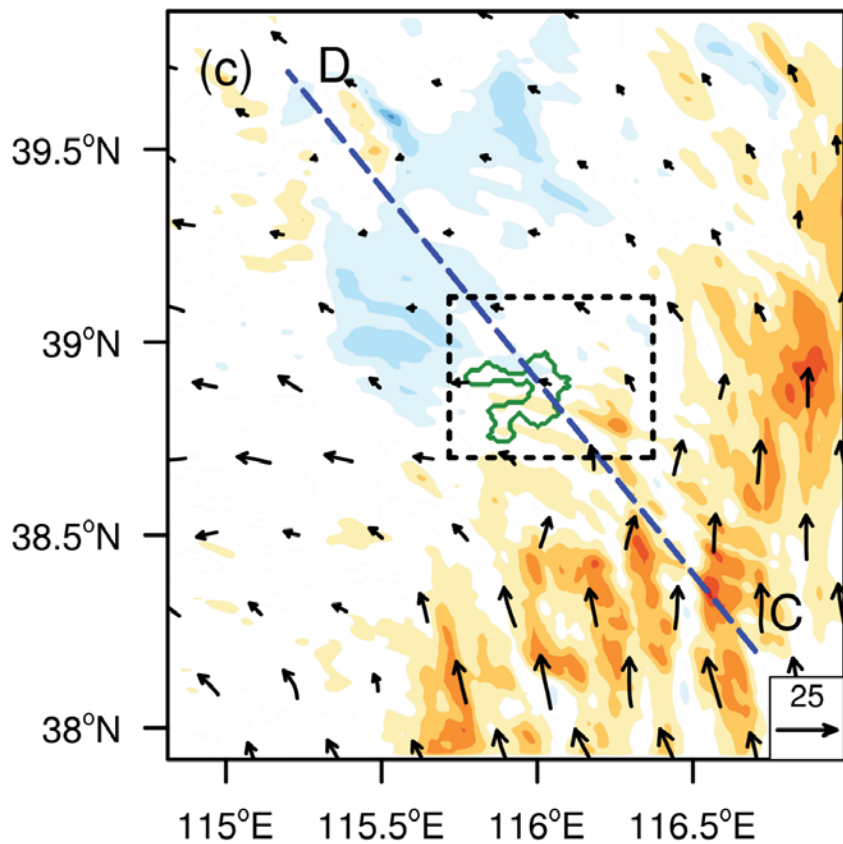
### CTRL-BASE

### URB-BASE

1st



2nd



Rainfall (mm)

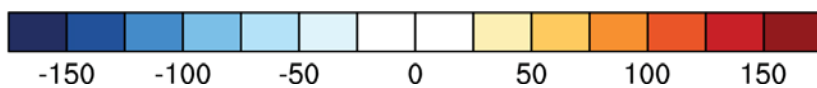


Figure 9.

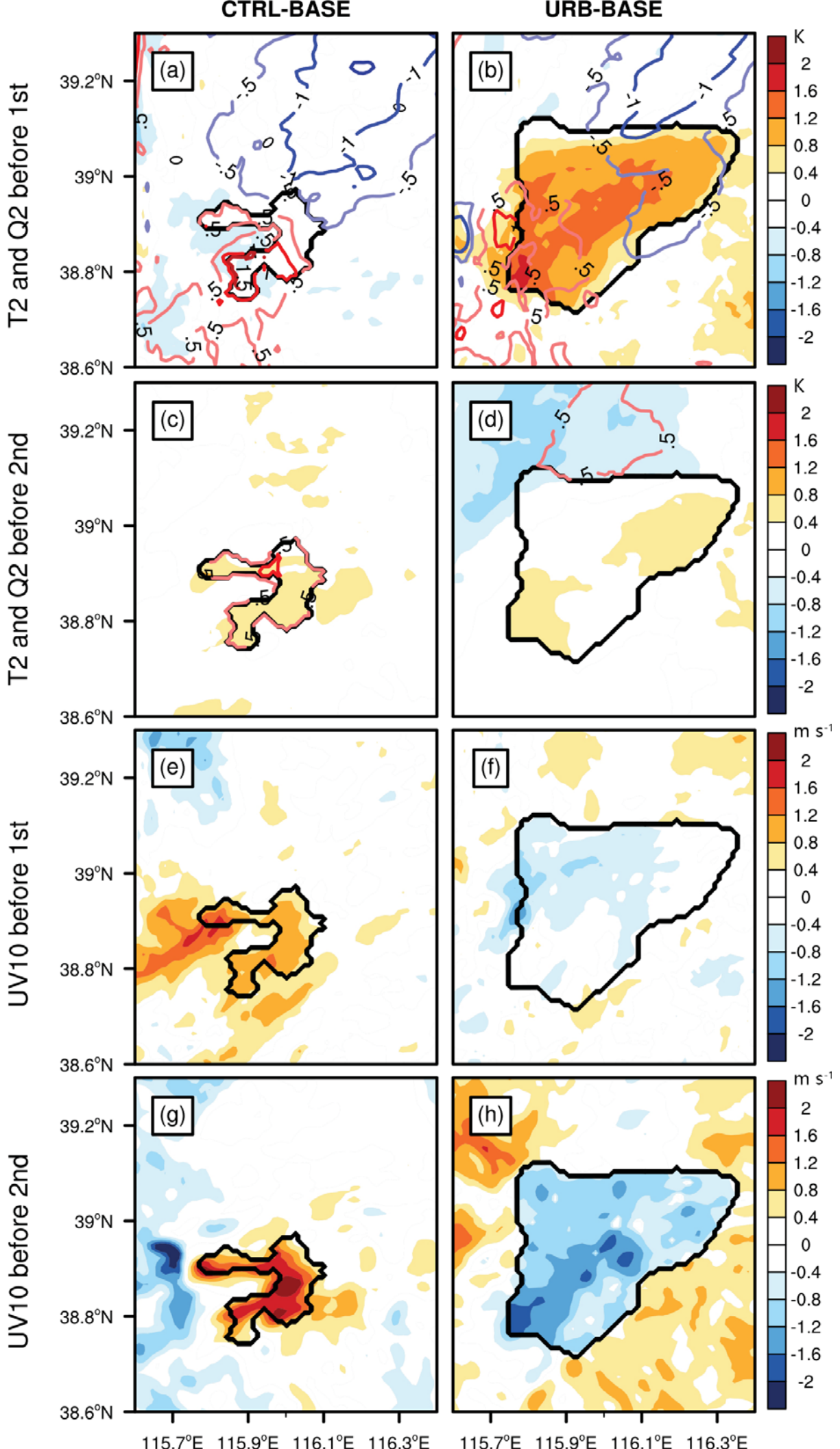


Figure 10.

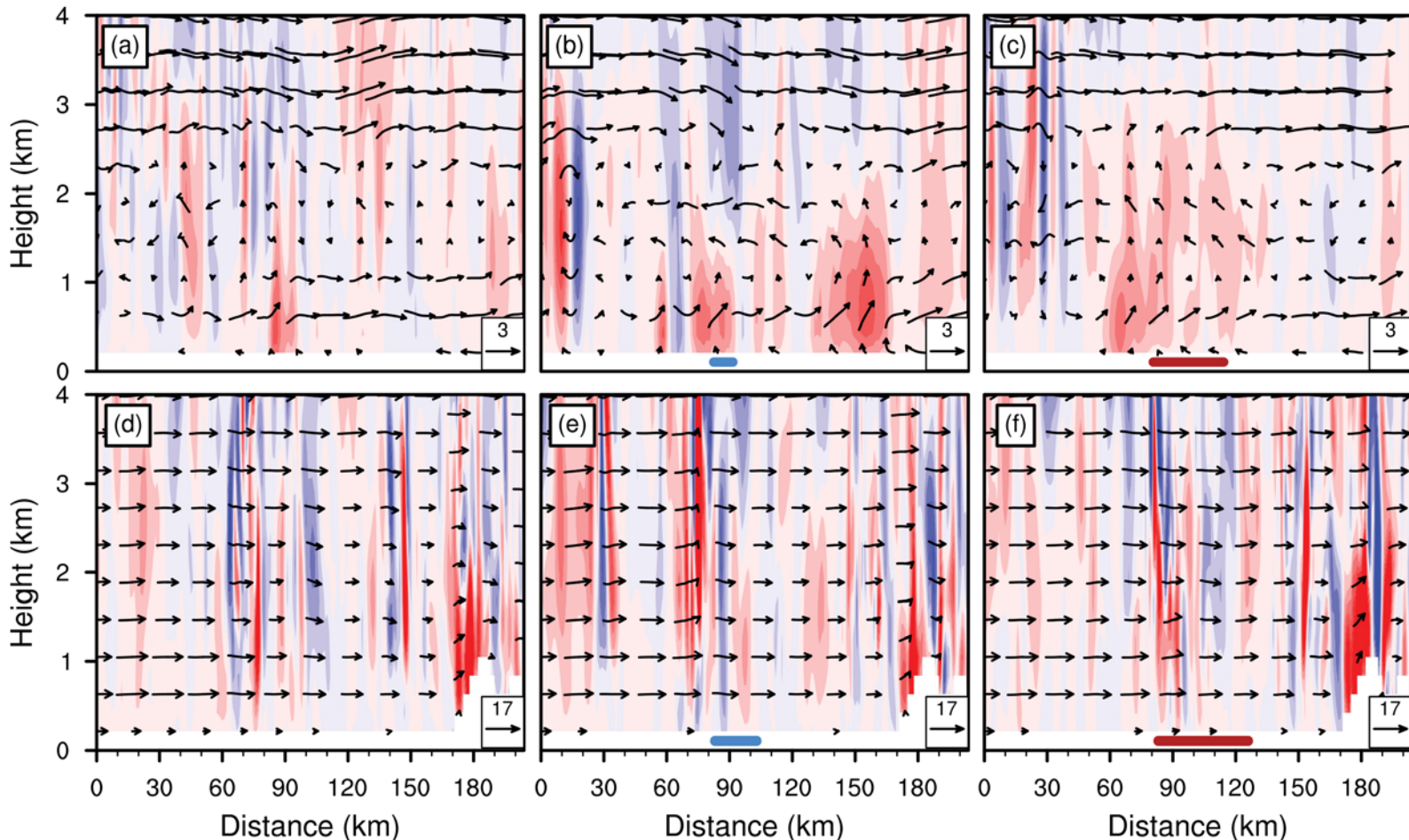
LineAB 17 UTC 18 July

LineCD 14 UTC 19 July

BASE

CTRL

URB



Wind Speed ( $\text{m s}^{-1}$ )



Figure 11.

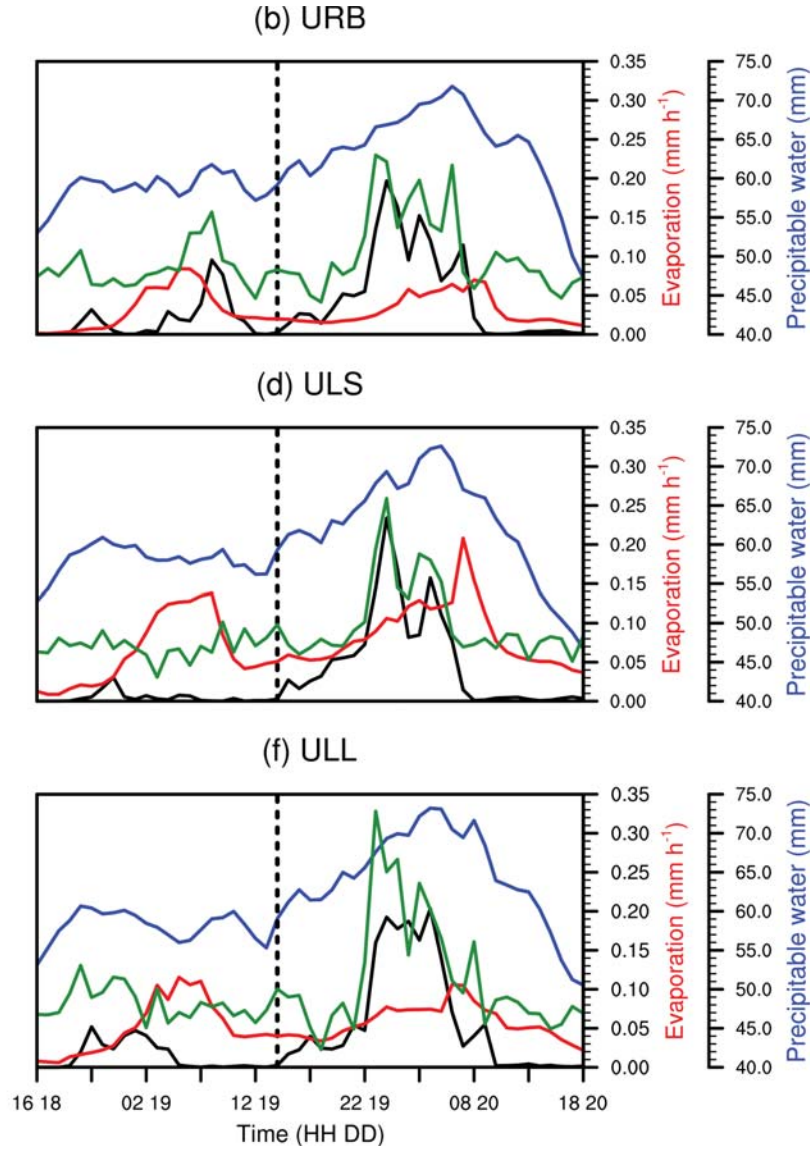
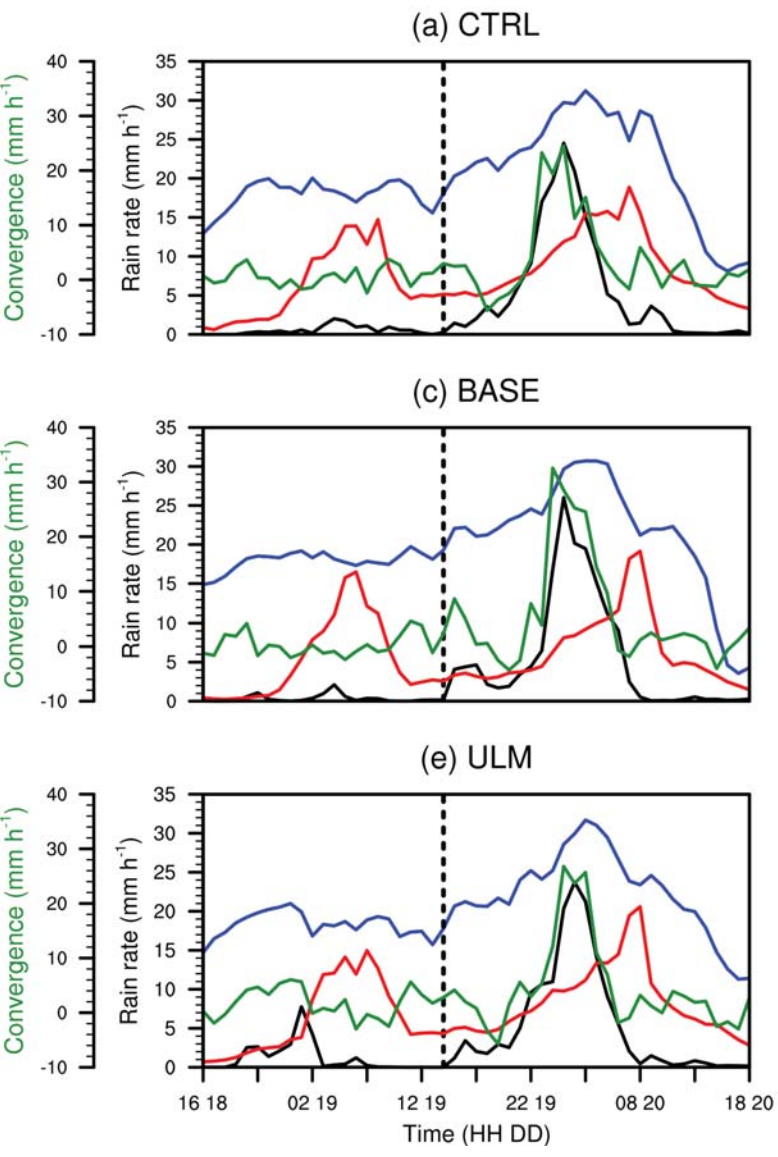


Figure 12.

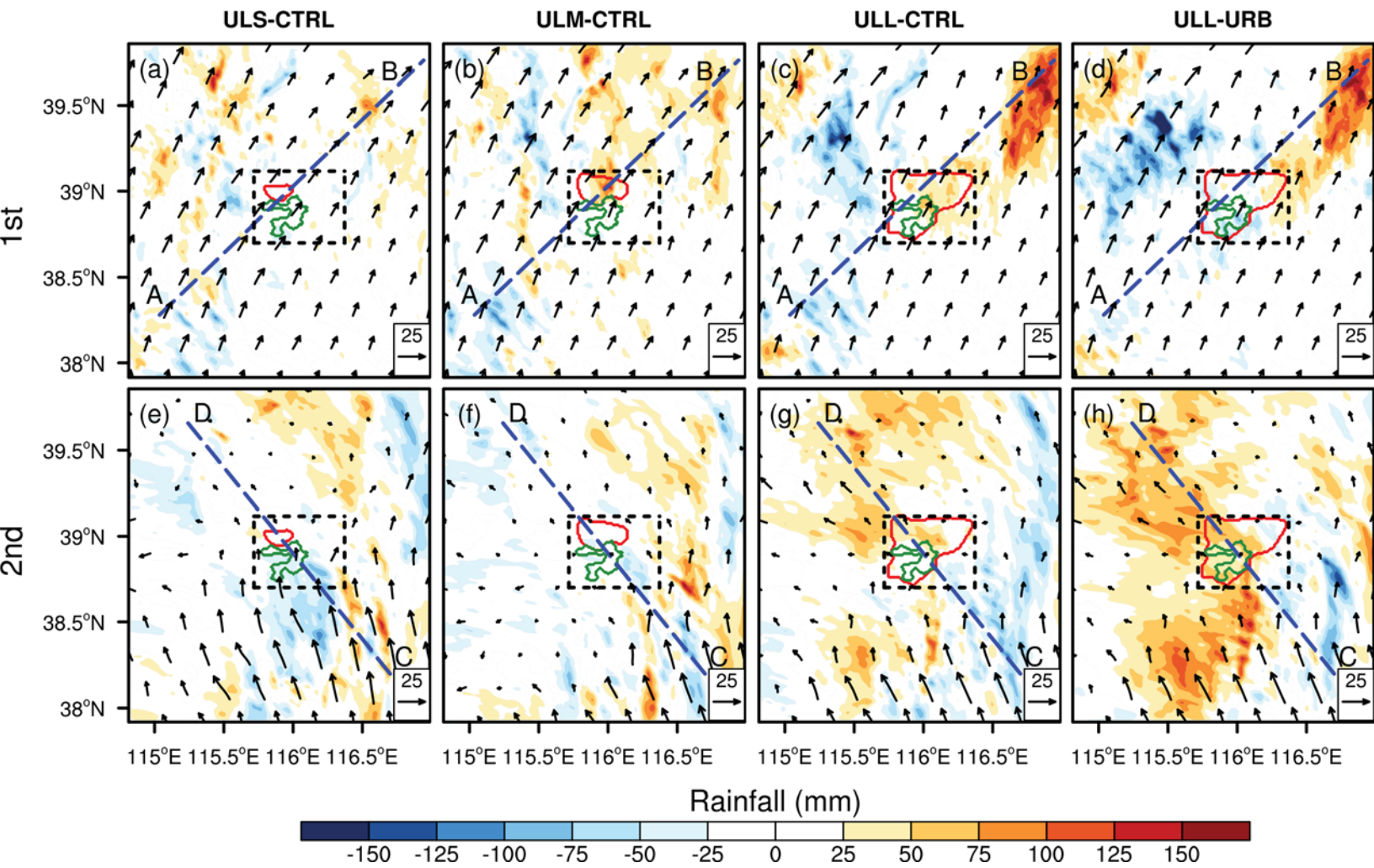


Figure 13.

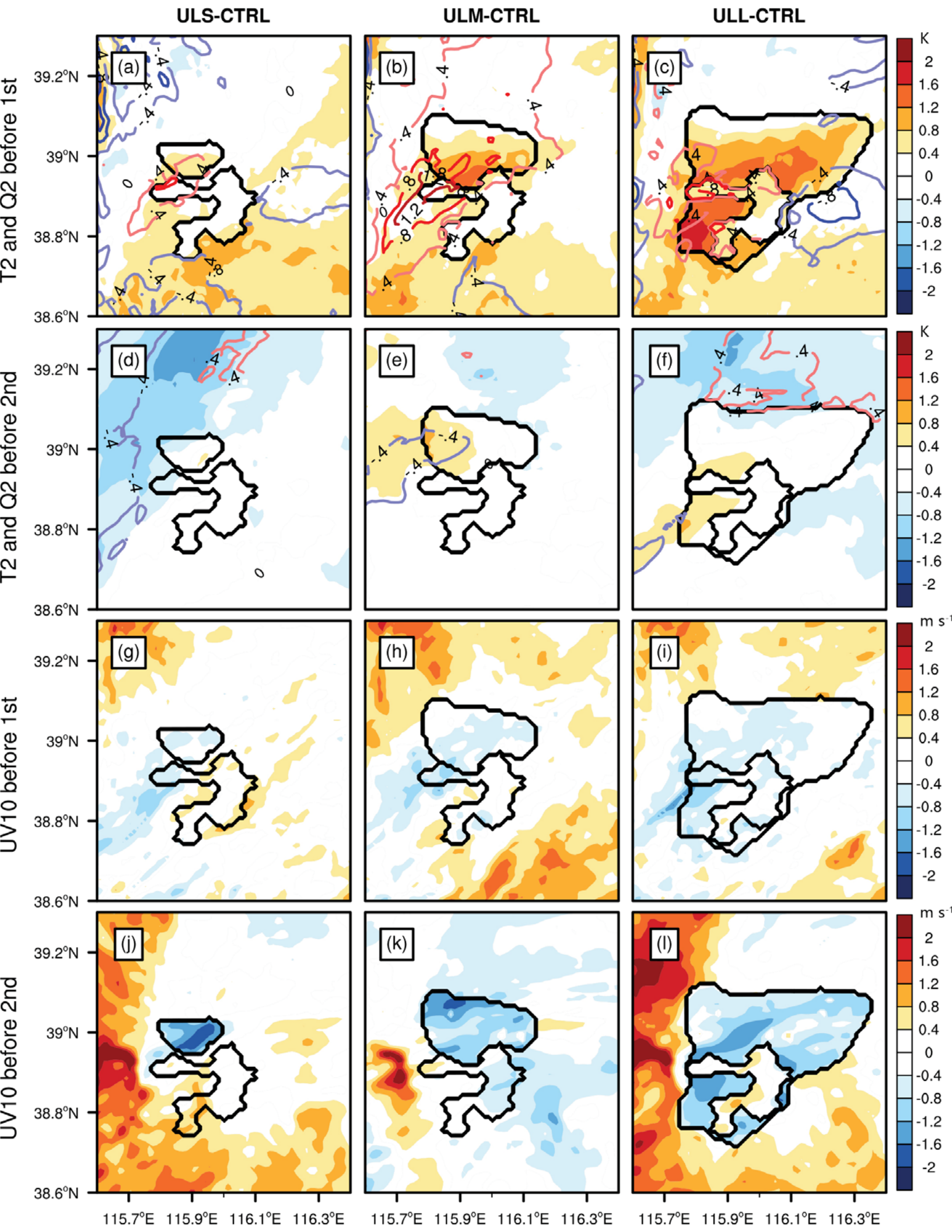
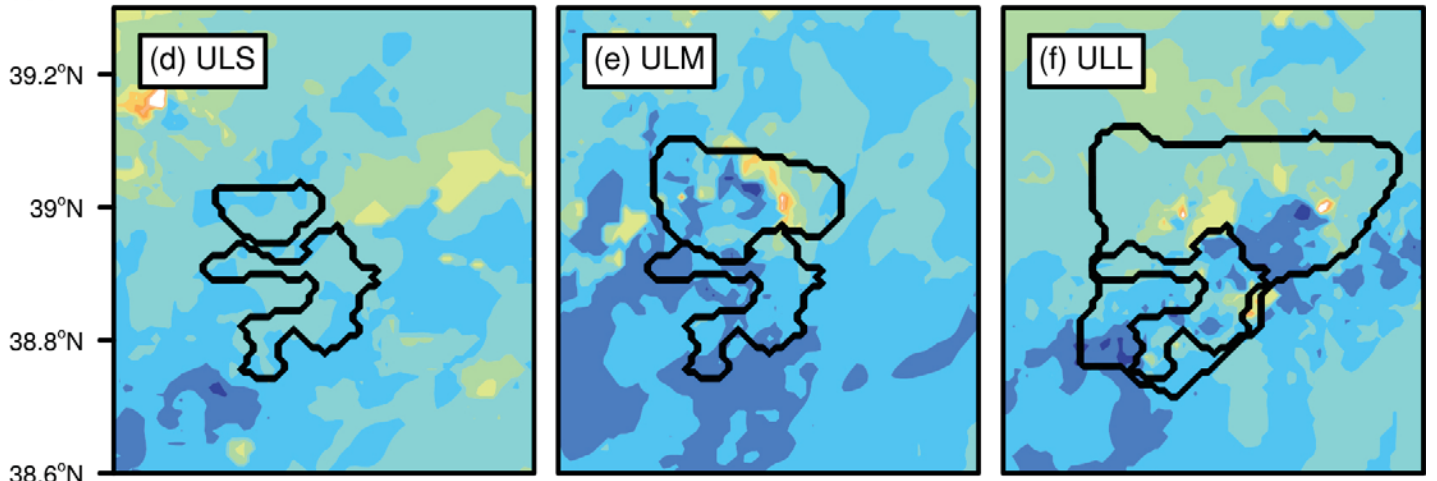
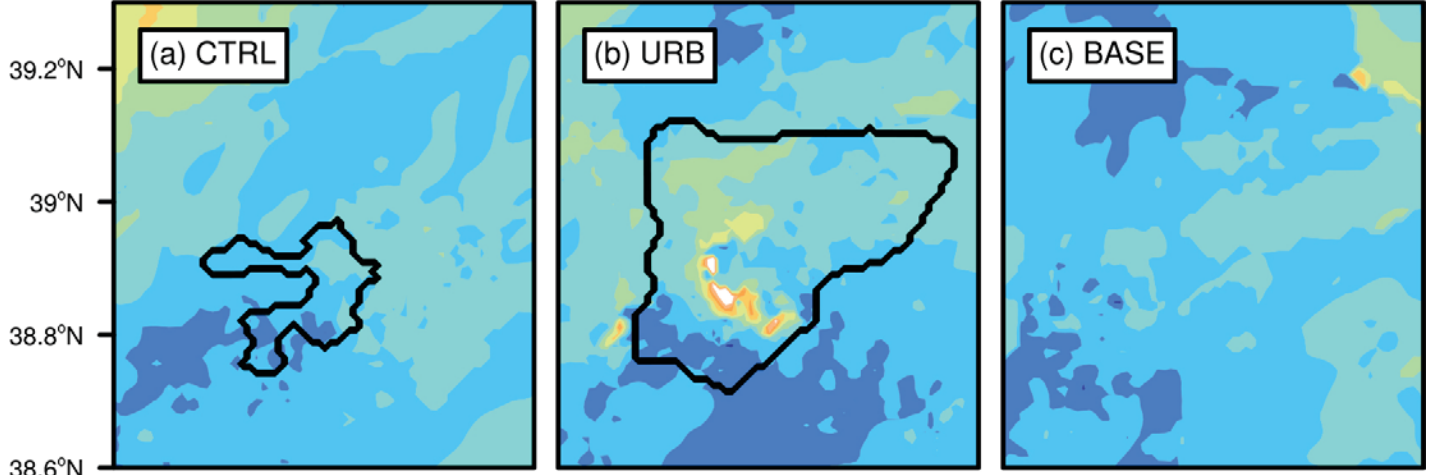
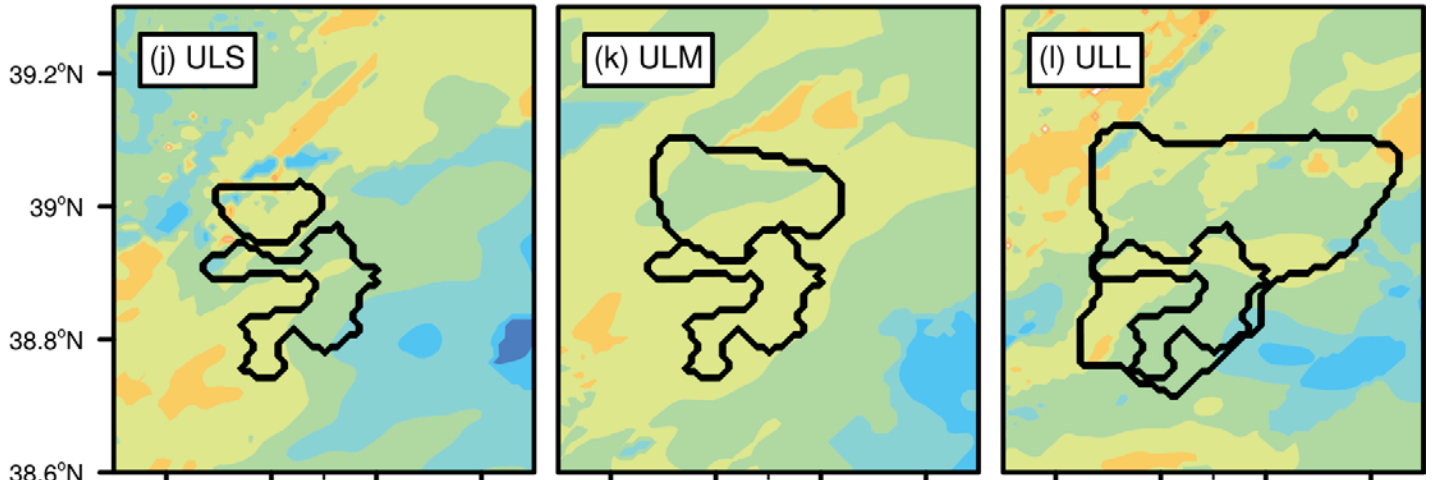
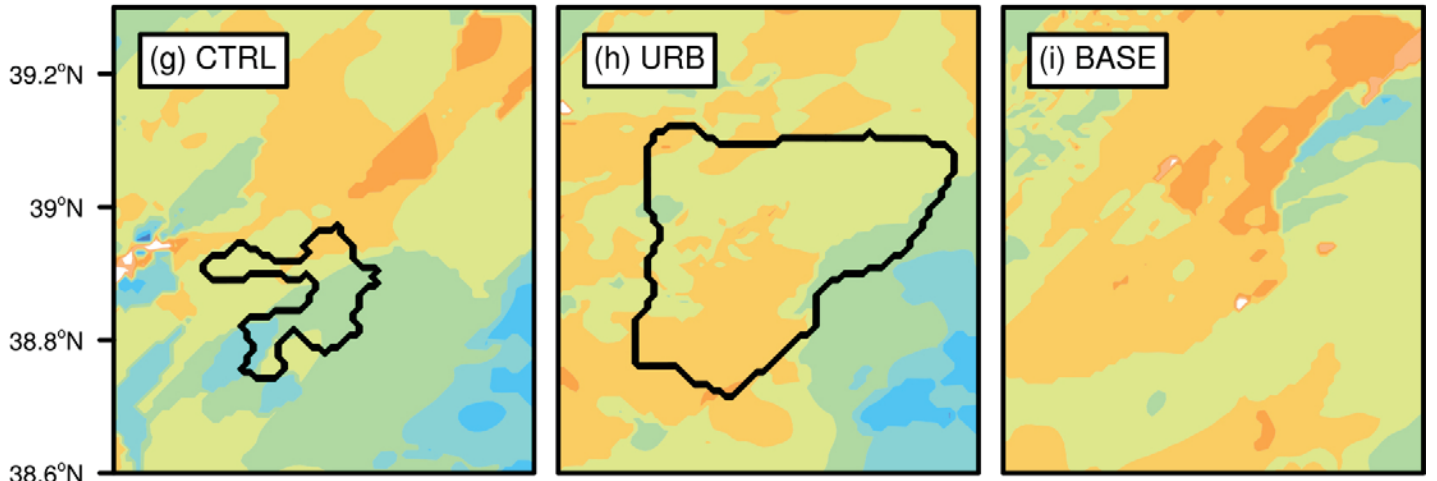


Figure 14.

20 UTC 18 July



12 UTC 19 July



115.7°E 115.9°E 116.1°E 116.3°E 115.7°E 115.9°E 116.1°E 116.3°E 115.7°E 115.9°E 116.1°E 116.3°E

Lifted Index

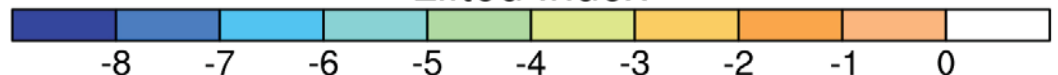


Figure 15.

LineAB 20 UTC 18 July

LineCD 12 UTC 19 July

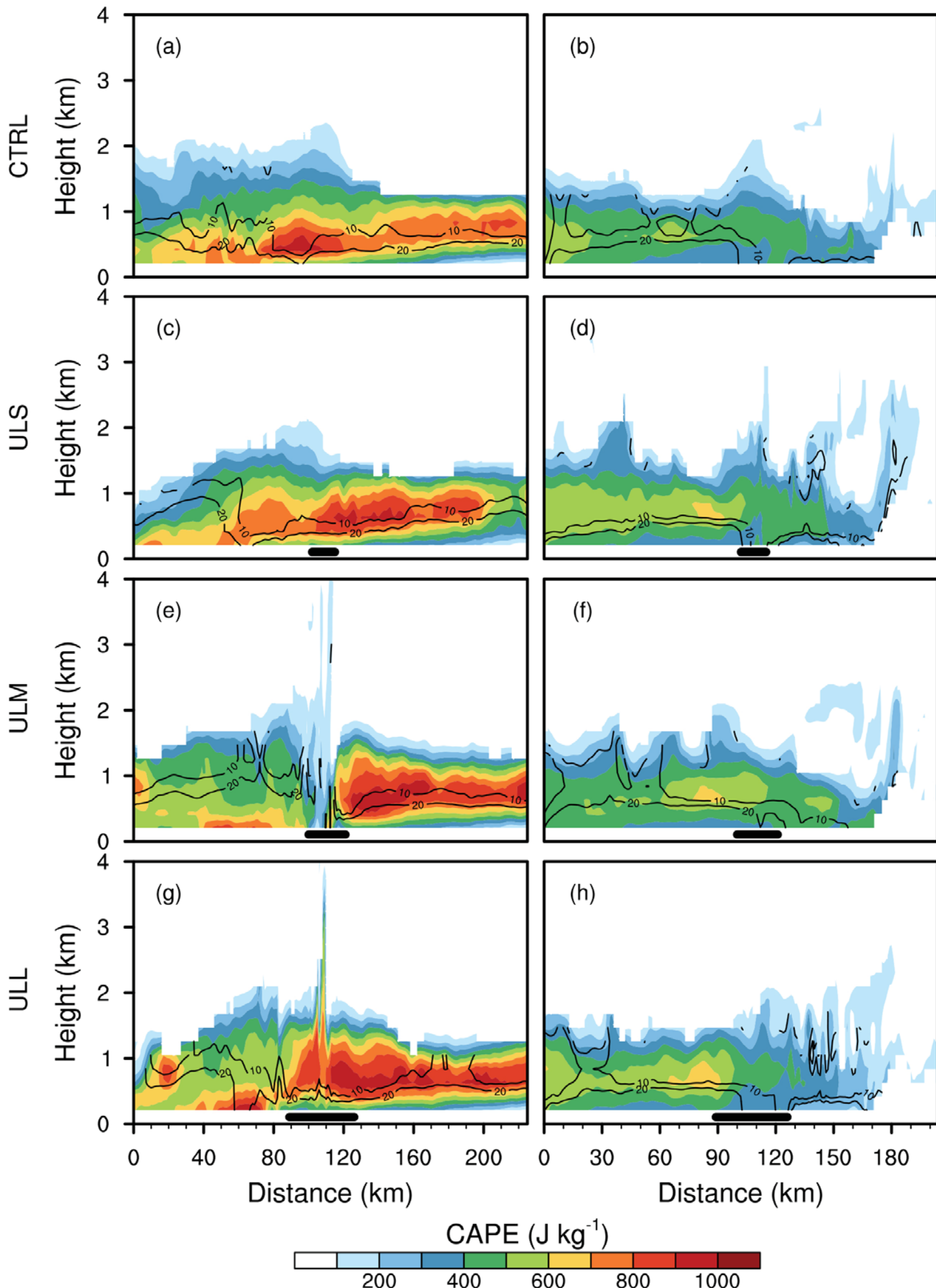


Figure 16.

LineAB

LineCD

